Department of Physics and Astronomy

University of Heidelberg

Diploma thesis
in Physics

submitted by
Georg Alexander Krocker
born in Ludwigshafen am Rhein, Germany

November 2009

Track reconstruction in the High Level Software Trigger of the LHC*b* experiment

This diploma thesis has been carried out by Georg Alexander Krocker at the
Physical Institute
under the supervision of
Prof. Dr. Stephanie Hansmann-Menzemer

Abstract

This work presents an optimisation of the track reconstruction of the final stage of the LHC*b* software trigger. This trigger stage fully reconstructs events to reduce the event rate from about 40 kHz to the final trigger output rate of 2 kHz.
Different scenarios of the online reconstruction are discussed. It is shown that a suppression of the output rate of 13% can be achieved without any loss in efficiency. The relative track finding efficiency between the offline and the online reconstruction can be improved by 5% by introducing two additional track reconstruction algorithms for reconstructing tracks in the vertex detector and for a redundant track search in the forward spectrometer.
By using a fast track fit optimised for online use and a more advanced primary vertex reconstruction algorithm the impact parameter resolution can be improved to almost the same quality as offline. The mass resolution of two prong B decays can be improved by a factor two.
Additionally, the origin of the remaining background on the trigger is discussed and possibilities to identify misreconstructed tracks are studied.

Kurzfassung

In dieser Arbeit werden Verbesserungen an der Spurfindung in der letzten Stufe des LHC*b* Software-Triggers vorgestellt. Diese Triggerstufe hat die Aufgabe die Ereignisrate von 40 kHz auf die endgültige Ausgaberate von 2 kHz zu reduzieren.
Verschiedene Szenarien der Onlinerekonstruktion werden diskutiert und es wird gezeigt, dass eine Reduzierung der Triggerrate um 13% bei gleich bleibender Signaleffizienz möglich ist. Die relative Spurfindungseffizienz zwischen der Offlinerekonstruktion und der Rekonstruktion im Trigger kann durch die Verwendung zusätzlicher Spurfindungsalgorithmen für die Rekonstruktion im Vertexdetektor und im gesamten Detektor um 5% gesteigert werden.
Durch Benutzung eines schnellen Spurfits, welcher speziell für die Verwendung im Trigger optimiert wurde, und einer verbesserten Primärvertexrekonstruktion lässt sich eine zur Offlinerekonstruktion vergleichbare Stoßparameterauflösung erreichen. Die Massenauflösung in Zweikörper B-Zerfällen verbessert sich um einen Faktor zwei.
Zusätzlich werden die Zusammensetzung der verbliebenen Untergrunds im Trigger analysiert und Möglichkeiten zur Identifikation von falsch rekonstruierten Spuren diskutiert.

Contents

Introduction

The Standard Model of particle physics, which has been introduced more than 30 years ago, describes the world of particles and antiparticles and their fundamental interactions. No laboratory experiment up to now has observed any significant deviation from the Standard Model.
Despite its huge success, physicists believe that the Standard Model is an effective theory only valid at energies studied up to now. A more fundamental theory is expected to be be revealed at higher energies.
There are many open question that the Standard Model ist not able to explain like, e.g., the evident excess of baryonic matter over antimatter in the universe or the existence of dark matter that is hinted by cosmological observations.
The Large Hadron Collider (LHC) at CERN, a 14 TeV proton-proton collider, was built to search for New Physics beyond the Standard Model. Three experiments are focussed on the search for new particles at the LHC: Direct searches are performed by the two multi purpose experiments ATLAS and CMS. The Large Hadron Collider beauty experiment (LHC*b*) is devoted to indirect searches for new particles via quantum corrections in loop processes. The potential reach of indirect searches is about an order of magnitude higher than direct searches. Most ground breaking findings in particle physics such as the existence of the charm quark or the third generation of quarks have first been observed in indirect searches.
The B meson system is an excellent laboratory for indirect searches, thus LHC*b* has been designed as a dedicated B physics experiment. Recent experimental results in the field of flavour physics such as the the assymetrie of particles and antiparticles in the B_s system by the CDF and DØ collaborations, although not yet statistically significant, show an interesting tension to the predictions of the Standard Model. With the production of 10^{12} B meson pairs within a year of running under nominal conditions, LHC*b* will significantly improve the existing measurements and potentially discover the first signature of New Physics.
To filter out interesting events from the vast background of hadronic interactions is one of the greatest challenges for the LHC*b* experiment. At the LHC, proton-proton bunches collide with a frequency of 40 MHz. Every hundredth collision produces a B meson pair which decays in up to five stable particles. In addition to these, 50 other particles from the underlying event are detected in the LHC*b* experiment. The LHC*b* trigger system reduces the rate from 40 MHz to 2 kHz for permanent storage. This reduction is performed in two steps. The first level is implemented in custom made hardware while the second level consists of dedicated software algorithms running on a CPU farm.
In this thesis, the track reconstruction for the final decision of the software trigger

is studied. At this level, a full event reconstruction as close as possible to the offline track reconstruction is performed. Any difference between the online and the offline track reconstruction strategies will introduce inefficiencies, thus understanding them is mandatory. A detailed analysis of these differences has been performed and potential improvements have been studied and implemented in the trigger software.
B mesons are triggered via their specific event topology, namely the long lifetime of the B meson as well as the relatively large momentum and transverse momentum of its decay particles. Therefore, the trigger relies heavily on the parameter estimate of the tracks as well as on information about the primary vertex of the events. The usage of a fast Kalman filter based track fit on the trigger as well as an improved primary vertex reconstruction algorithm has been studied in this thesis.
In addition, the composition of the background after the final trigger selection has been analyzed as a starting point for further efforts on the suppression of this background.

Chapter 1

Physics programme of the LHC*b* experiment

The Standard Model of particle physics sucessfully describes todays knowledge about the elementary particles and their interactions. To probe the Standard Model and search for possible deviations from its predictions is the goal of the LHC*b* experiment. Flavour physics is one of the most promising fields in the search for New Physics because new particles can occour virtually in loop processes. Through these loop processes, energies way beyond the scope of todays collider experiments become accessible.
This section gives an brief introduction to the Standard Model and CP violation in the Standard Model. It further gives an overview about some of the key physics channels in the LHC*b* experiment, that provide distinctive tests of the Standard Model already with the very first data.

1.1 The Standard Model

The Standard Model distinguishes two types of elementary particles: fermions, which have half integer spin, and bosons, which have integer spin. Fermions are the building blocks of matter while bosons act as force carriers that mediate the interactions between the fermions.
The fermions are divided into leptons and quarks both of which can be subdivided into

Table 1.1: Fermion content of the Standard Model: quarks and leptons. The approximate particle masses are given in parentheses [1].

	type	1^{st} generation	2^{nd} generation	3^{rd} generation
leptons	neutrino	ν_e ($< 2\,\text{eV}$)	ν_μ ($< 2\,\text{eV}$)	ν_τ ($< 2\,\text{eV}$)
	lepton	e (511 keV)	μ (106 MeV)	τ (1.78 GeV)
quarks	up	u (2 MeV)	c (1.25 GeV)	t (174 GeV)
	down	d (5 MeV)	s (95 MeV)	b (4.2 GeV)

three generations with increasing mass. Each generation consists of two fermions. The reason why there are exactly three generations is not yet understood and is considered as a possible hint to a theory beyond the Standard Model.
For the quarks, the three generations with two types of quarks result in six quark flavours, *u*p, *d*own, *s*trange, *c*harm, *b*ottom and *t*op quark. The LHC*b* experiment is particularly interested in the physical properties of mesons composed of the bottom or beauty quark.
The three generations of leptons each contain a charged lepton and a neutral lepton, the neutrino. The charged leptons are electron, muon and tau. The neutrinos are massless in the Standard Model. However, recent discoveries in the measurement of the solar neutrino flux show that the neutrinos have a small but finite mass.
In addition to the mentioned particles, each particle also has an anti-particle with opposite charge. The *CPT* theorem, a fundamental theorem of quantum gauge theory, states that the fundamental particles and interactions are invariant under subsequent application of the charge conjugation (C), parity transformation (P) and time inversion (T) operators. One conclusion of the *CPT* theorem is that particles and anti-particles, which are connected through the charge conjugation operator, must have the same mass and decay time.
All Standard Model fermions have been observed today. Besides the fermions, the

Table 1.2: Boson content of the Standard Model and the approximate particle mass and relative strength of the corresponding interaction [1].

interaction	(gauge) bosons	mass	relative strength
Strong	gluons ($g_1, \ldots, g_8$)	0	$\alpha_s \sim \mathcal{O}(1)$
Electromagnetic	photon (γ)	0	$\alpha \sim \mathcal{O}(10^{-2})$
Weak	$W^{\pm}$	80 GeV	$\alpha_W \sim \mathcal{O}(10^{-6})$
	Z^0	91 GeV	
—	Higgs boson (H^0)	> 114 GeV	–

Standard Model predicts the existence of five bosons: the photon as propagator of the electromagnetic force, the $W^{\pm}$ and Z^0 boson to carry the weak force, the gluon for the strong force and the Higgs boson. The Higgs boson has not yet been observed, the search for its existence is one of the key goals of the ATLAS and CMS experiment at the LHC.
The electromagnetic force acts on the quantum number *charge* through an exchange of a photon. Charged leptons have charge $Q = -1$ their anti-particles have charge $Q = 1$. The up-type quarks (u, c, t) have charge $Q = 2/3$, the down-type quarks (d, s, b) have $Q = -1/2$. The anti-quarks respectively have the sign-flipped charge of the quarks.
The strong force acts on a quantum number of the quarks named *colour*. The quarks can have three different colours as well as the respective anti colours for anti-quarks. The theory of the strong force, the Quantum Chromo Dynamics (QCD) only allows colour neutral objects composed of quarks. Thus, quarks can only occur in bound

states, so called hadrons. Two types of hadrons are possible, the mesons, which are composed of a quark and an anti-quark with the corresponding anti-colour and baryons with a combination of three quarks which are of different colour or anti-quarks which are of different anti-colour.
The weak force is acting on all fermions via the exchange of a charged $W^{\pm}$ boson, the so called charged current, or a neutral Z^0 boson. The exchange of a $W^{\pm}$ boson changes charged leptons into neutrinos or up-type quarks into down-type quarks or vice versa, the exchange of the Z^0 boson cannot change the flavour of the quarks.
The electromagnetic and weak force can be unified in an electroweak theory. An additional boson, the Higgs boson H^0, is necessary to explain the symmetry breaking that leads to the masses of both the $W^{\pm}$ and Z^0 bosons in contrast to massless photon.

1.2 CP violation in the Standard Model

After the unification of the electromagnetic and weak forces and the symmetry breaking, the fermions couple to the scalar Higgs field as well and so, obtain masses. However, the mass eigenstates are not identical to the eigenstates of the weak force. The transformation that transforms the mass eigenstates (d, s, b) of the quarks to the corresponding weak eigenstates (d', s', b') can be written in the form of the 3×3 matrix $\boldsymbol{V}_{\mathrm{CKM}}$ such as

$$\mathbf{q}' = \boldsymbol{V}_{\mathrm{CKM}}\mathbf{q} \tag{1.1}$$

with the *Cabibbo-Kobayashi-Maskawa* CKM mixing matrix

$$\boldsymbol{V}_{\mathrm{CKM}} = \begin{pmatrix} V_{ud} & V_{us} & V_{ub} \\ V_{cd} & V_{cs} & V_{cb} \\ V_{td} & V_{ts} & V_{tb} \end{pmatrix}. \tag{1.2}$$

Each entry in the CKM matrix can potentialy be a complex number, leading to a total of 18 parameters. By definition the CKM matrix must be unitary which leads to 9 constraints. The five relative phases of the weak and the mass eigenstates of the quark fields can be reduced to one phase by redefining the fields. This leaves a total of three real rotational angles and one phase. The remaining phase is the sole source of *CP* violation in the Standard Model. The CKM matrix can be re-parametrized with the four remaining parameters by a power-series expansion in the sine of the *Cabibbo-angle* Θ_c, $\lambda = \sin\Theta_c \approx 0.22$:

$$\boldsymbol{V}_{\mathrm{CKM}} = \begin{pmatrix} 1 - \frac{\lambda^2}{2} & \lambda & A\lambda^3(\rho - i\eta) \\ -\lambda & 1 - \frac{\lambda^2}{2} & A\lambda^2 \\ A\lambda^3(1 - \rho - i\eta) & -A\lambda^2 & 1 \end{pmatrix} + \mathcal{O}(\lambda^4). \tag{1.3}$$

The unitarity of $\boldsymbol{V}_{\mathrm{CKM}}$ leads to the condition that the sum of the entries in one row or collumn must be equal to one which can be visualized as triangles in the complex plane. Altogether, six triangles can be constructed from the unitarity constraint of the CKM matrix. Two of these triangles have sides in the same order of magnitude, the others are degenerated. One non-degenerated triangle is defined by the unitarity condition

$$V_{ud}V_{ub}^* + V_{cd}V_{cb}^* + V_{td}V_{tb}^* = 0. \tag{1.4}$$

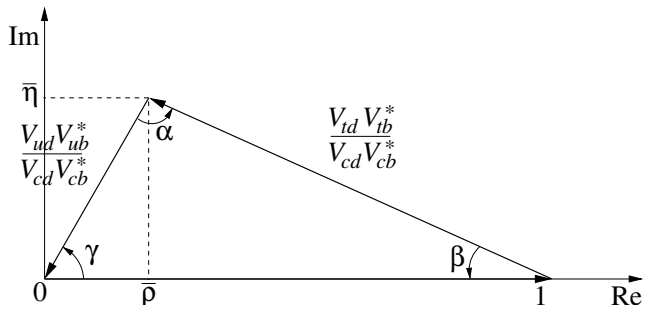

Figure 1.1: Scheme of the unitarity triangle in the complex plane. The base line is normalized to unity (Figure from [2].)

Figure 1.1 shows this unitarity triangle with the base length normalized to one. The three angles are given by

$$\alpha = arg(-\frac{V_{td}V_{tb}^*}{V_{ud}V_{ub}^*}), \quad \beta = arg(-\frac{V_{cd}V_{cb}^*}{V_{td}V_{tb}^*}), \quad \gamma = arg(-\frac{V_{ud}V_{ub}^*}{V_{cd}V_{cb}^*}). \tag{1.5}$$

The area of the unitarity triangle is the same for each one and gives a direct measurement of the amount of *CP* violation in the Standard Model. Many New Physics models predict effects that would lead to additional CP violation in the flavour sector. Thus, by constraining the matrix elements of the CKM matrix and searching for deviations from the Standard Model predictions, one can find possible evidence for New Physics. The status of these measurements is summarized in figure 1.2. All measurements done so far are compatible with the Standard Model expectations. However, one can see that a precise measurement of the angle γ is still missing, which results in a large uncertainty for the upper edge of the unitarity triangle. The precise measurement of γ is one of the key goals for the LHC*b* experiment.

Another interesting measurement is the one of the unitarity triangle

$$V_{us}V_{ub}^* + V_{cs}V_{cb}^* + V_{ts}V_{tb}^* = 0\,. \tag{1.6}$$

One of the angles in this triangle is the angle β_s, which is defined as

$$\beta_s = \arg\left(-\frac{V_{ts}V_{tb}^*}{V_{cs}V_{cb}^*}\right). \tag{1.7}$$

Both triangles of $b-s$ and $b-d$ transitions are accessible via a measurement of the mixing of neutral B mesons. In total there are four neutral B mesons:

$$|B_d\rangle = |\bar{b}d\rangle \quad , \quad |\overline{B}_d\rangle = |b\bar{d}\rangle \tag{1.8}$$

$$|B_s\rangle = |\bar{b}s\rangle \quad , \quad |\overline{B}_s\rangle = |b\bar{s}\rangle. \tag{1.9}$$

The mixing between the $|B_s\rangle$ and $|\overline{B}_s\rangle$ (or $|B_d\rangle$ and $|\overline{B}_d\rangle$) occurs because the mass eigenstates of the B meson are not identical to the eigenstates of the weak interaction. The time development of the flavour eigenstates is described by the time dependent *Schrödinger equation*

$$i\frac{d}{dt}\begin{pmatrix} B_s \\ \overline{B}_s \end{pmatrix} = (M - \frac{i}{2}\Gamma)\begin{pmatrix} B_s \\ \overline{B}_s \end{pmatrix}. \tag{1.10}$$

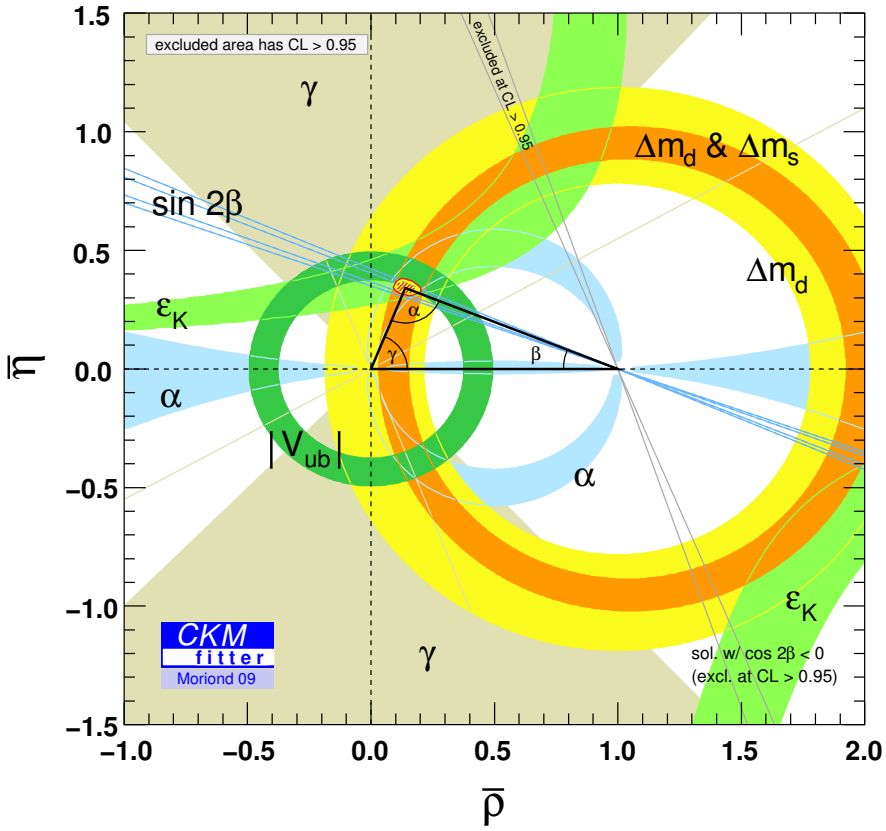

Figure 1.2: Global fit of all measurements contributing to $\boldsymbol{V}_{\mathrm{CKM}}$. (Figure from [3].)

The two parameters M and Γ are Hermitian 2×2 matrices where the diagonal elements are the masses and decay times of the flavour eigenstates. According to the *CPT* theorem, they are equal for particles and anti-particles and thus $M_{11} = M_{22}$ and $\Gamma_{11} = \Gamma_{22}$. The off-diagonal elements satisfy $M_{12} = M_{21}^*$ and $\Gamma_{12} = \Gamma_{21}^*$. They are determined by the mixing between the flavour eigenstates. The leading order Feynman diagrams for the mixing in the B_s system are shown in figure 1.3.
The eigenstates of the Schrödinger equation 1.10 are the mass eigenstates of the neutral B mesons, given by

$$B_L = p|B_s\rangle + q|\overline{B}_s\rangle \tag{1.11}$$
$$B_H = p|B_s\rangle - q|\overline{B}_s\rangle \tag{1.12}$$

whereas the ratio q/p is obtained by solving the Schrödinger equation as

$$\frac{q}{p} = -\sqrt{\frac{M_{12}^* - i\Gamma_{12}^*/2}{M_{12} - i\Gamma_{12}/2}}\,. \tag{1.13}$$

If the ratio $|q/p|$ is unequal to one the probability of the transition $B_s \to \overline{B}_s$ differs from the probability of the transition $\overline{B}_s \to B_s$. So, the mixing process violates the *CP* symmetry. However, the Standard Model predicts the *CP* violation in mixing to be

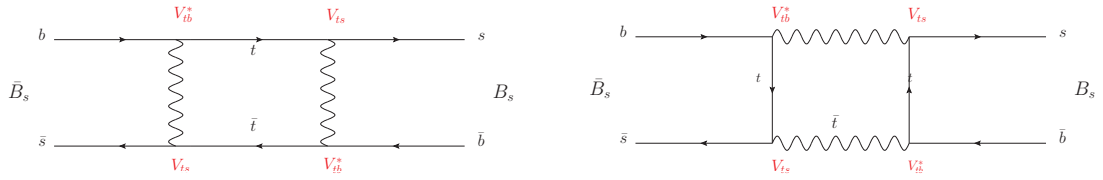

Figure 1.3: The dominant diagrams for the $B_s - \overline{B}_s$ mixing.

very small as there is only one dominating diagram for this process.
Another possibility is that the decay of a B meson into some final state f itself may be *CP* violating, meaning that the probability of a B going to a final state f is unequal to the probability of the $\overline{B}$ going to the final state $\overline{f}$,

$$\frac{\langle f|B_s\rangle}{\langle \overline{f}|\overline{B}_s\rangle} \neq 1\,. \tag{1.14}$$

This form of *CP* violation has been measured e.g. in the decay $\mathrm{B_d} \to \mathrm{K^+\pi^-}$by the *BABAR* [4] and the *Belle* [5] experiments.
Finally, *CP* violation can occur if there is a relative phase between q/p and $\langle f|B_s\rangle/\langle f|\overline{B}_s\rangle$, i.e. in the interference between decay and mixing. If this is the case, the *CP* violation can be measured in the weak mixing phase, defined as

$$\Phi_s = \arg\left(\frac{q}{p}\frac{\langle f|B_s\rangle}{\langle f|\overline{B}_s\rangle}\right)\,. \tag{1.15}$$

Additional *CP* violation introduced by New Physics can appear in all three sectors, hence they will all be studied for different decay channels in the LHC*b* experiment.
The Standard Model prediction [6] for the weak mixing phase Φ_s in the B_s system is

$$\Phi_s = -2\beta_s = (-0.0368 \pm 0.0017)\,\mathrm{rad}, \tag{1.16}$$

where β_s is the angle from the $b-s$ CKM triangle defined in equation 1.7. The decay mode $\mathrm{B_s} \to \mathrm{J/\psi\phi}$ is in particular interesting for a measurement of the weak mixing [7] phase since the time dependend *CP* assymetrie $A_{CP}(t)$ is proportional to $\sin\Phi_s$. A measurement of this assymetrie will give direct access to the angle β_s.
The CDF and DØ collaborations presented results on the measurement of the weak mixing phase in the decay $\mathrm{B_s} \to \mathrm{J/\psi\phi}$ that show a possible deviation from the Standard Model [8–10]. The current combined HFAG result [11] is

$$\Phi_s = [(-0.77^{+0.29}_{-0.37}) \text{ or } (-2.36^{+0.37}_{-0.29})]. \tag{1.17}$$

The expected statistical sensitivity for LHC*b* on Φ_s has been estimated to be

$$\mathcal{L} = 0.5\,\mathrm{fb}^{-1} \;:\; \sigma(\Phi_s) = 0.060 \pm 0.005\,, \tag{1.18}$$

$$\mathcal{L} = 2.0\,\mathrm{fb}^{-1} \;:\; \sigma(\Phi_s) = 0.030 \pm 0.002\,. \tag{1.19}$$

Systematical errors have been studied and found to be smaller than the statistical uncertainty for $2\,\mathrm{fb}^{-1}$. With already very few data, LHC*b* will be able to either confirm the deviation from the Standard Model expectation or show that the current result is a statistical fluctuation.

1.3 Rare decays of B mesons

Decays that have a low branching fraction in the Standard Model are an excellent probe of possible New Physics. Many of the New Physics models predict new particles which lead to additional contributions in the transition matrix element. Thus, if there is a theory beyond the Standard Model, the branching fraction of such decays should deviate from the prediction of the Standard Model.
One particularly interesting example is the decay $B_s \to \mu^+\mu^-$[12]. This decay requires a flavour changing neutral current, which is forbidden at tree level in the Standard Model. The lowest order Feynman diagram allowed in the Standard Model, a electroweak penguin diagram, is depicted in Figure 1.4 (a). Since the B_s meson is a pseudoscalar meson, the both leptons from the decay must be either both left handed or both right handed, which leads to an additional helicity suppression. As a result, the expected Standard Model branching fraction is very small. It is predicted to be

$$\mathcal{BR} = (3.35 \pm 0.32) \times 10^{-9}\,. \tag{1.20}$$

The current experimental limit on this branching ratio from the CDF and DØ experiments [13] is

$$\mathcal{BR} < 4.7 \cdot 10^{-8}\,. \tag{1.21}$$

at 90% confidence limit.
In New Physics models such as, e.g., the Minimal Supersymmetric Standard Model

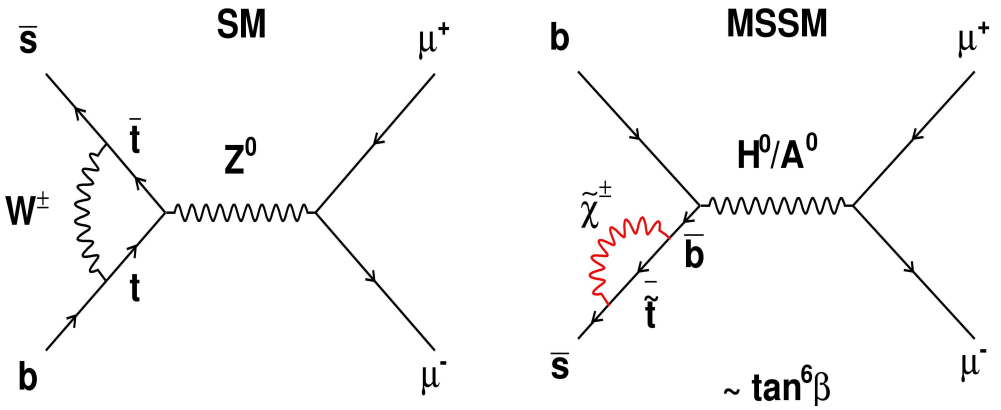

(a) Standard Model (b) MSSM

Figure 1.4: Examples of Feynman diagrams contributing to the decay $B_s \to \mu^+\mu^-$. (a) in the Standard Model and (b) in the Minimal Supersymmetric Model (figure from [12]).

(MSSM), the branching fraction is enhanced due to new particles contributing to the decay. An example of such a contribution is shown in figure 1.4 (b), were the $\bar{s} \to b\bar{b}$ transition is mediated via a loop with a tauino and a neutralino, two supersymmetric particles, and the decay is propagated via the neutral Higgs bosons H^0/A^0. In the MSSM the $B_s \to \mu^+\mu^-$branching ratio could exceed the Standard Model value by as much as 10^3. Even if no evidence for a branching ratio above the SM expectations is found, a enhancement on the upper limit of the branching fraction of $B_s \to \mu^+\mu^-$will help to constrain the parameter space of supersymmetric models.

Chapter 2

The LHC*b* experiment

The LHC*b* experiment is one of six experiments at the Large Hadron Collider, a proton proton synchrotron located at CERN in Geneva. The collider is designed for a center of mass energy of 14 TeV. First collision are foreseen at the end of 2009.
At the LHC*b* experiment, proton bunches cross with a rate of 40 MHz. The rate of visible interactions, i.e. the rate of inelastic proton proton collisions with at least five tracks inside the acceptance range of the detector, is a function of the instantaneous luminosity, which is determined by the proton density in the bunches. In Figure 2.1 (a) the probability for one or multiple interactions as a function of the luminosity is shown. At nominal running conditions, about 0.7 collisions per bunch crossing take place leading to a rate of 14 MHz of visible interactions. The integrated luminosity of one year (10^7 s) under nominal running conditions is $\mathcal{L} = 2\,\mathrm{fb}^{-1}$.
In Figure 2.1 (b) the angle between the b or $\bar{b}$ produced in an proton proton collision at the LHC and the z-axis, i.e. the direction of the beam, is shown. It can be seen that both B mesons produced in such a collision fly either in the forward or backward direction. That is the reason why the LHC*b* detector is designed as a single arm forward spectrometer. About 25% of all B events lie in the acceptance of the detector.
A technical sketch of the LHC*b* detector is shown in figure 2.2. It covers an acceptance of $10-300$ mrad in the bending plane of the magnet (x-z) and $10-250$ mrad perpendicular to that plane. The detector elements can be categorized in tracking detectors, particle identification detectors, calorimeter system and muon detectors. Since mainly tracking detectors are of interest for this thesis, the focus will be put on their description.

2.1 Tracking system

The main tracking system consists of the vertex detector (Velo) the trigger tracker (TT) and the three tracking stations (T-Stations), which are composed of the inner tracker (IT) and the outer tracker (OT). The dipole magnet lies between the the trigger tracker and the T-Stations. Charged particles are bent in the field of the magnet so as to be able to calculate their momentum from the deflection. The main component of the magnetic field is oriented in the y direction. So, particles moving through the detector are deflected in the (x-z) plane. The magnet was designed in such a way that the other components of the magnetic field are negligible for most purposes. The integrated

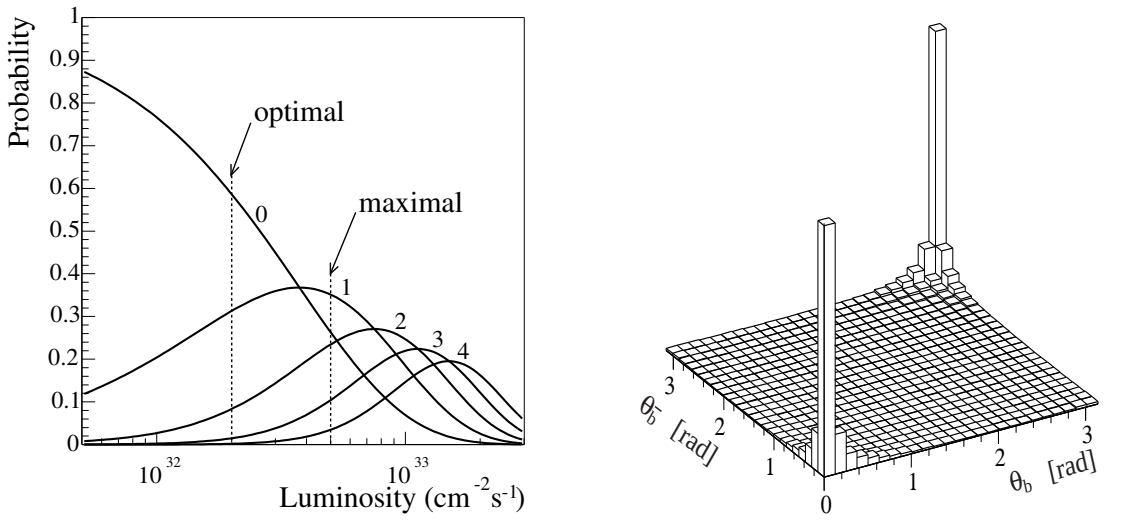

(a) Probability for multiple interactions (b) Correlation between b and $\bar{b}$ polar angles

Figure 2.1: (a) Probability of the different number of interactions as a function of the luminosity. At nominal luminosity 0.7 inelastic proton proton collisions per bunch crossing take place in the detector. Optimal and maximal design luminosities are indicated by dashed lines. (b) Angle between the flight direction of a B or $\overline{B}$ produced in a proton proton collision and the z-axis [14].

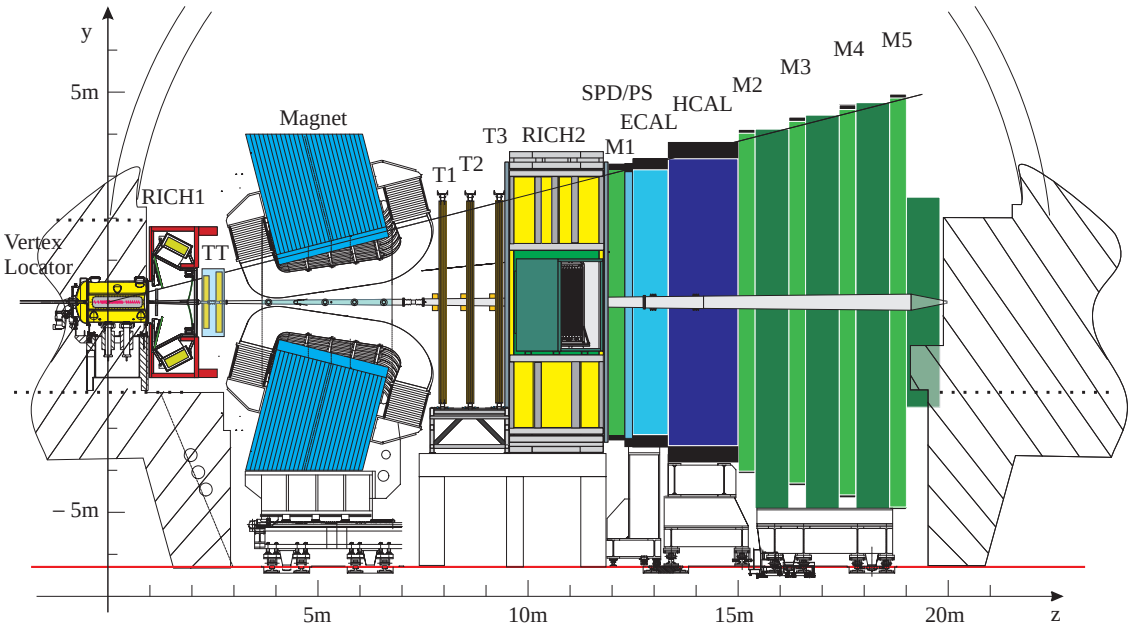

Figure 2.2: Side view of the LHCb detector layout in the (y-z) plane. Detector elements from left to right are: The Vertex Locator (Velo), the first RICH detector, the trigger tracker (TT), the dipole magnet, the tracking stations T1-T3 (T-Stations), RICH 2, the first muon station (M_1), the Scintillating Pad Detector (SPD), Preshower (PS), Electromagnetic (ECal) and Hadronic (HCal) calorimeters and the muon stations $M_2 - M_5$ [14].

magnetic field is

$$\int Bdl = 4.2\,\mathrm{Tm}\,. \tag{2.1}$$

The direction of the field can be flipped, thus providing the possibility to check if there are any effects on the reconstruction from detector asymmetries.

2.1.1 Vertex Detector

The vertex detector is built of two types of silicon based strip detectors. Sensors with strips around the beam pipe measure the r component of a hit, while sensors in radial direction measure the ϕ component[1]. The two types of sensors are mounted on half disc silicon chips which are positioned on both sides of the beam line. The sensitive area of the silicon chips starts at 8 mm from the beam and extends to 96 mm. As it can be seen from Figure 2.4 the pitch of both r and ϕ sensors increases from the beam line outwards to obtain an homogeneous particle flux. The average occupancy per sensor is below 1%. The sensor modules are positioned in 21 stations on both sides of the beam line as indicated in figure 2.3.
The special design of the Velo sensors is used by the trigger: Tracks from secondary vertices can be first reconstructed in the (r-z) plane and have a characteristically high impact parameter with respect to the primary vertex. This method of finding events with such long lived particles is very efficient in terms of CPU time.
Since the Velo is very close to the beam line, there is a specific danger of damaging the sensors in case of a defocused or lost beam. Therefore the two halves of the Velo can be moved away from the beam line during the injection of the beam until a stable beam condition is reached. The two halves of the Velo are separated from the beam line by a thin aluminium foil, which shields the Velo electronics from electric currents induced by the beam and prevents a gas exchange between the vacuum of the Velo and the LHC machine. The design of the Velo provides a reconstruction of the primary interaction region with a precision of about 40 μm in the (x-y)plane.

2.1.2 Trigger Tracker

The trigger tracker is composed of four layers of silicon strip detectors. Two layers respectively form one station, the two stations are 27 cm apart. The TT is located directly in front of the magnet. Because the silicon strips of the TT point in y direction, the best resolution is reached in the bending plane of the magnet as can be seen in Figure 2.5. The second and the third layer, the so called u and v layers are tilted with respect to the y axis to a stereo angle of -5 deg and $+5$ deg to provide a three dimensional reconstruction of the tracks. The spatial resolution of the TT is about 50 μm.

2.1.3 Tracking Stations

The three tracking stations (T-Stations) provide information about the particle trajectories behind the magnet. They consist of two detectors, the inner tracker (IT) and the

[1] ϕ is the azimuthal angle of a polar coordinate system along the z-axis.

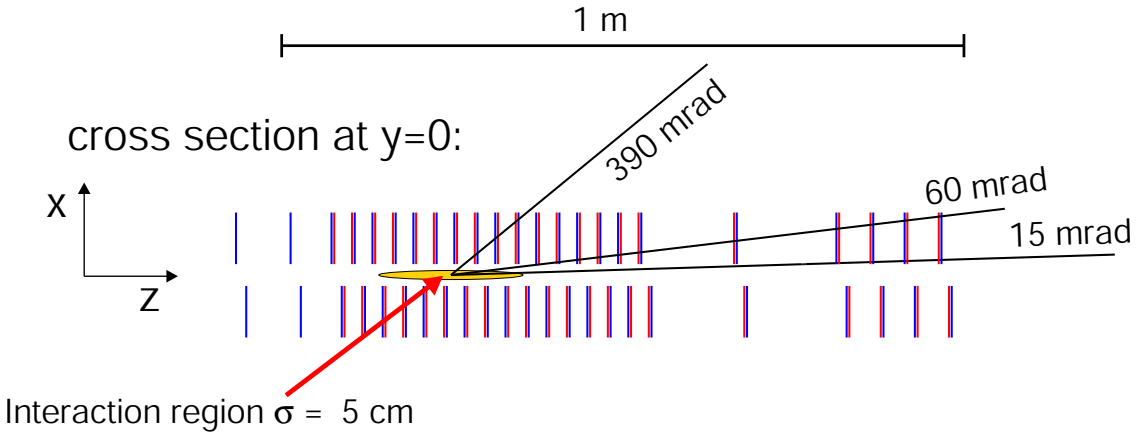

Figure 2.3: Setup of Velo modules around the interaction region [14].

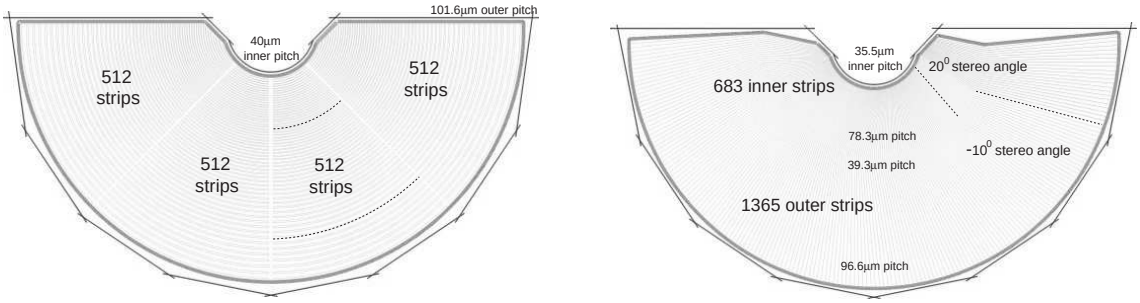

(a) r–sensor (b) ϕ–sensor

Figure 2.4: Sketch illustrating the $r - \phi$ geometry of the Velo sensors. The different regions on the sensors are indicated with their pitch [14].

outer tracker (OT).

The inner tracker [15] is located in the central region of the T-Stations in a cross shaped geometry around the beam pipe. Figure 2.6 shows a technical sketch of the IT. Due to its position around the beam pipe the inner tracker receives about 20% of the total particle flux in the T-Stations, although it covers only 2% of the area. The IT therefore uses silicon sensors to obtain a maximal occupancy of 2%. In each of the three tracking stations, the IT consists of four layers. Two stereo layers are enclosed by two x layers in a similar configuration as in the TT.

The outer region of the T-Stations are covered by the outer tracker [16]. The outer tracker is a drift tube gas detector. It consists of four layers per tracking station, which are arranged in the same geometry with x and stereo layers as in the IT. Figure 2.7 (a) shows a front view of one T-Station. It can be seen that each layer is composed of 14 long modules and 8 short modules that are arranged around the IT. Charged particles are detected by their ionization in the straw tube drift chambers. Figure 2.7 (b) illustrates of the arrangement of the drift straws in an OT module. The straws have an inner diameter of 5 mm, the pitch between two straws is 5.25 mm. The nominal counting gas in the OT is a mixture of Ar and CO_2 in the volume ratio 70 / 30 per

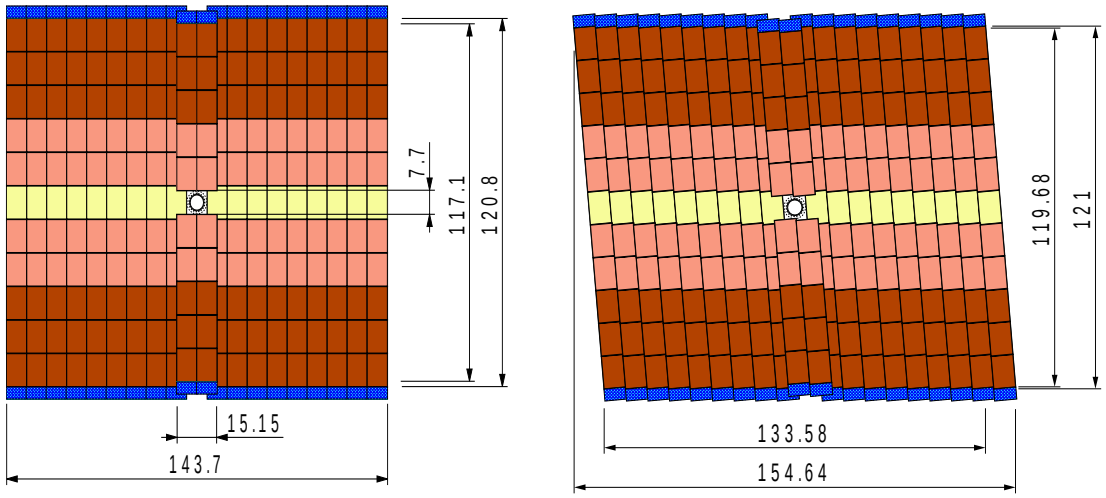

(a) TT x layer (b) TT stereo layer

Figure 2.5: Layout of the Trigger Tracker: (a) x layer and (b) stereo layer. The different colours indicate the different sensor readouts. Dimensions in the figure are given in cm [14].

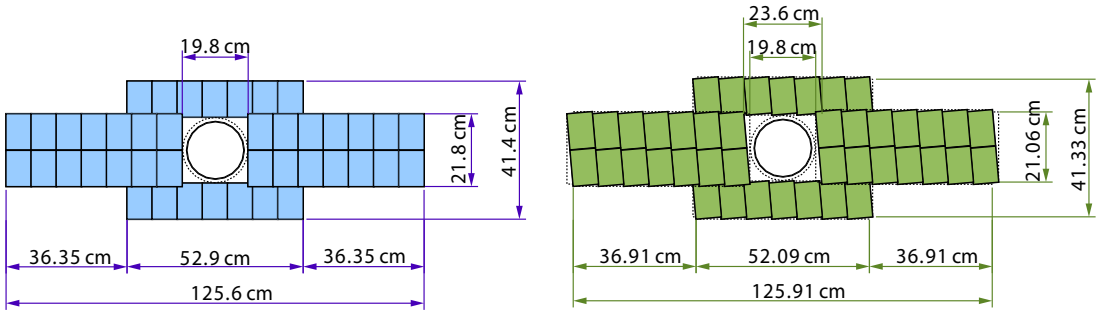

Figure 2.6: Layout of an Inner Tracker x and u layer with the silicon sensors in the cross shaped configuration. In the middle, the cross section of the beam pipe is drawn [2].

cent.
The OT has a very high efficiency of 98% and provides a spacial resolution better than 200 μm [17].

2.2 Calorimeter System

The calorimeter system [18] is used for energy measurement and particle identification. It further provides information about the position of neutral particles that leave no hits in other subdetectors. The calorimeter information is used in the offline reconstruction as well as in the hardware trigger system. In Figure 2.8 a sketch of the calorimeter system is shown. It consists of a preshower element, an electromagnetic and a hadronic calorimeter.

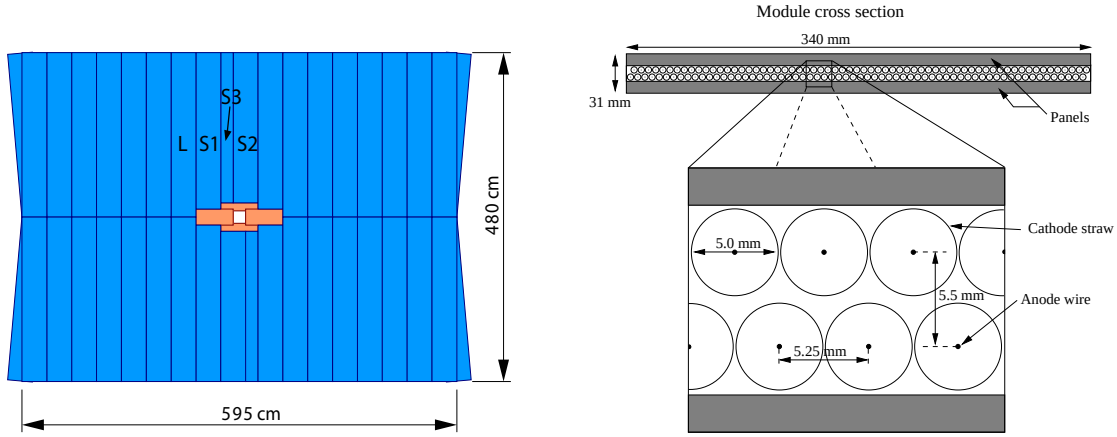

(a) front view of the T-Stations

(b) OT module with straws

Figure 2.7: Outer tracker: (a) Front view of an OT station. The four boxes in the center depict the IT. (b) Cross section of an OT module (128 straws). A small region containing a few straws is magnified [2].

The Scintillating Pad Detector (SPD) and the Preshower Detector (PS) are used for particle identification. Charged particles interact with the scintillating material of the SPD, while neutral particles do not. Electrons and photons start to shower an electromagnetically in the 12 mm thick lead wall behind the SPD. This shower is detected in the scintillating pads of the PS. Since the combination of SPD, lead wall and PS amounts to 2 electromagnetic interaction lengths, but only 0.1 hadronic interaction lengths, hadrons, electrons and photons can be distinguished by the signal they leave in the Pre-Shower Detector.
The electromagnetic calorimeter (ECAL) is designed as a shashlik calorimeter with 66 alternating layers of 2 mm lead and 4 mm scintillating plates. This corresponds to 25 electromagnetic interaction lengths and 1.1 hadronic interaction lengths. It is designed to offer an energy resolution of

$$\sigma(E)/E = 10\,\%/\sqrt{E} \oplus 1.5\,\%\,, \tag{2.2}$$

where the energy E is given in GeV and $\oplus$ means addition in quadrature.
The hadronic calorimeter consists of alternating layers of scintillating tiles and iron as absorber material. The light from the scintillators is fed to photomultiplier tubes via optical fibres. The hadronic calorimeter is in total 5.6 hadronic interaction lengths long. It provides an energy resolution of

$$\sigma(E)/E = 80\,\%/\sqrt{E} \oplus 10\,\%. \tag{2.3}$$

2.3 RICH detectors

The two Ring Imaging Cherenkov Detectors RICH 1 and RICH 2 should offer information to identify hadrons. They make use of the fact that a particle traversing a medium

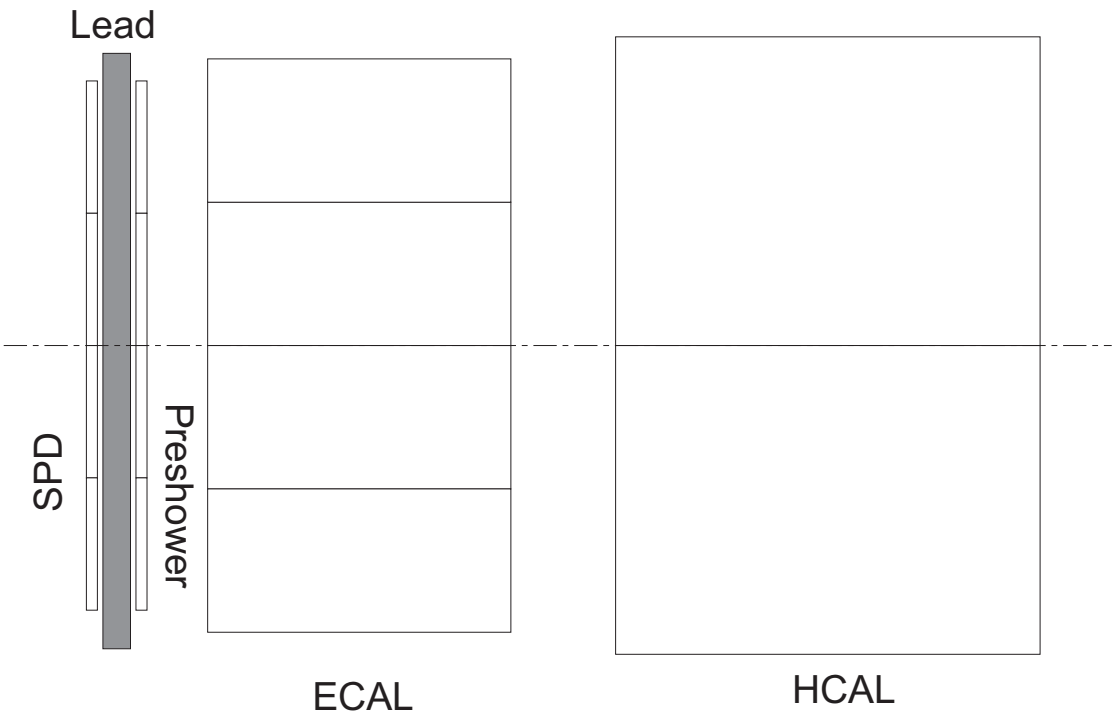

Figure 2.8: Schematic side view of the calorimeter system [19].

radiates light on a cone around its trajectory if its velocity is higher than the speed of light in this medium. The opening angle of this cone is determined by

$$\cos\theta = 1/n\beta \tag{2.4}$$

where n is the refractive index in the medium. In LHCb, three different radiation media are used, Aerogel and C_4F_{10} in RICH 1 and CF_4 in RICH 2. Due to the different refractive indices of the materials used, low momentum particles up to 60 GeV are identified using RICH 1 in front of the trigger tracker, while high momentum particles up to 100 GeV are detected with RICH 2 behind the T-Stations. The Cherenkov light produced by the particles is reflected by a mirror system and detected via Hybrid Photo detectors (HPD)[2] in RICH 1 and via photomultiplier tubes in RICH 2.
The reconstruction of the Cherenkov rings in the RICH detectors is very time consuming and therefore not used in the trigger.

2.4 Muon stations

The muon detectors [20] consist of five stations with the first station M1 located in front of the calorimeter and M2-M5 behind the HCAL. Between M2 to M5 iron plates with a thickness of 80 cm are placed. They correspond to 20 electromagnetic interaction

[2] An HPD is a combination of a vacuum tube and a silicon detector. Photo-electrons are accelerated with a high voltage onto a silicon chip were they produce an ionization cluster. This cluster can be detected.

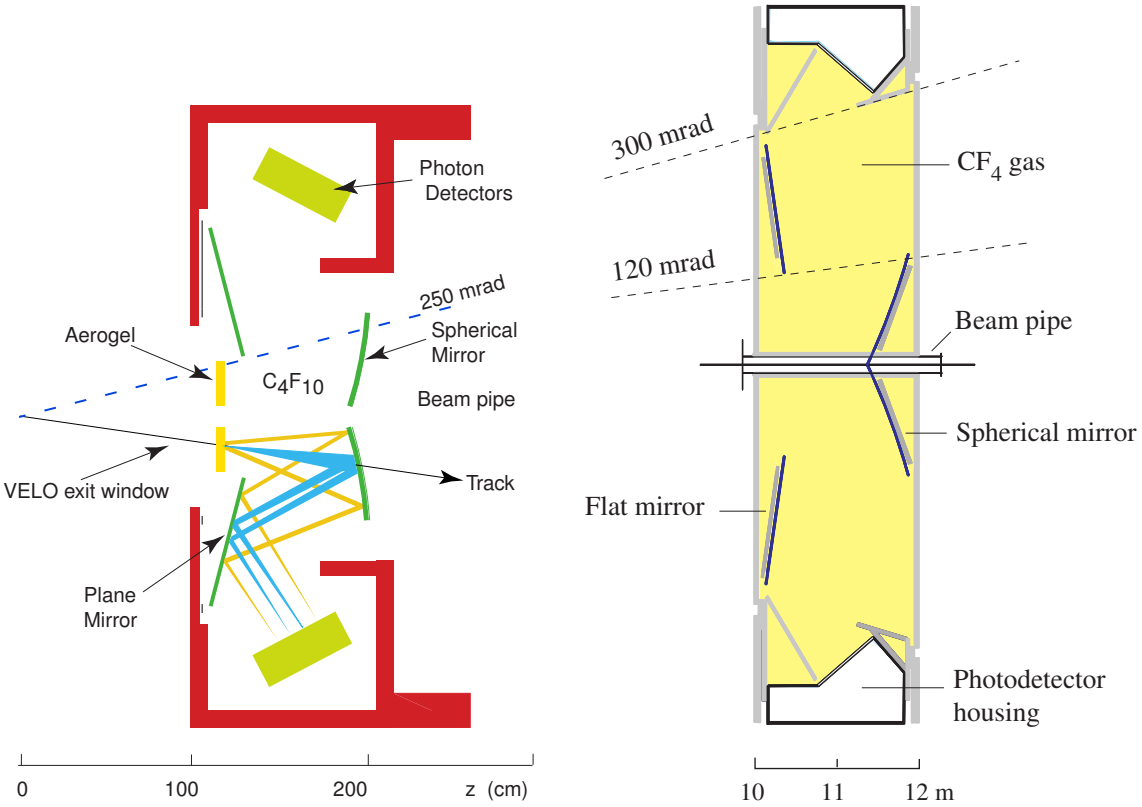

(a) RICH 1 (b) RICH 2

Figure 2.9: RICH detectors: (a) Schematic view of RICH 1. (b) Schematic view of RICH 2. The principles of the detection of Cherenkov light emitted by particles is indicated for RICH 1 [14].

lengths. Muons are detected via multiwire proportional chambers which provide a fast readout for the hardware trigger system. In M1, GEM detectors are used around the beam pipe where the particle flux is higher.
The muon system is used in the L0 software trigger to identify high momentum muons that have hits in all five muon stations. This requires the muon to have a minimal momentum of about 6 GeV.

2.5 Trigger system

The LHCb trigger system consists of two stages. The first stage is the L0 hardware trigger, which reduces the rate from the bunch crossing rate of 40 MHz to about 1 MHz using information from the muon detectors and the calorimeter system. At the L0 output rate, a full readout of the detector is possible. The second stage is the High Level Software trigger (HLT), a `C++` application running on a computing cluster. The HLT is divided into two levels. The first level (HLT1) performs a confirmation of the L0 trigger objects. It reduces the rate from 1 MHz to about 40 kHz. At the second level (HLT2), a full event reconstruction as similar as possible to the offline reconstruction is performed. This way the rate is reduced to the final trigger output rate of 2 kHz.

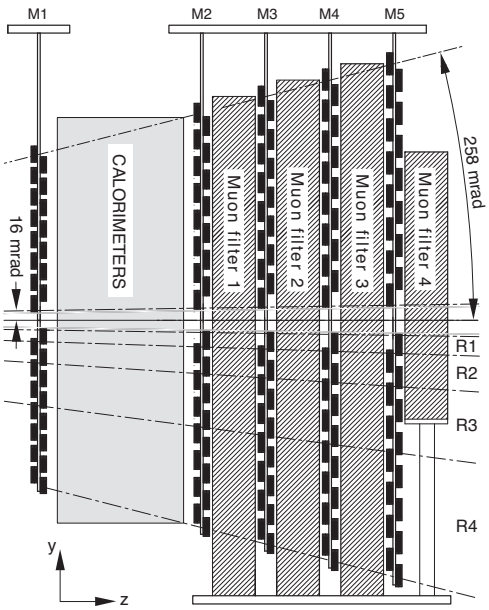

Figure 2.10: Muon System: Side view [14].

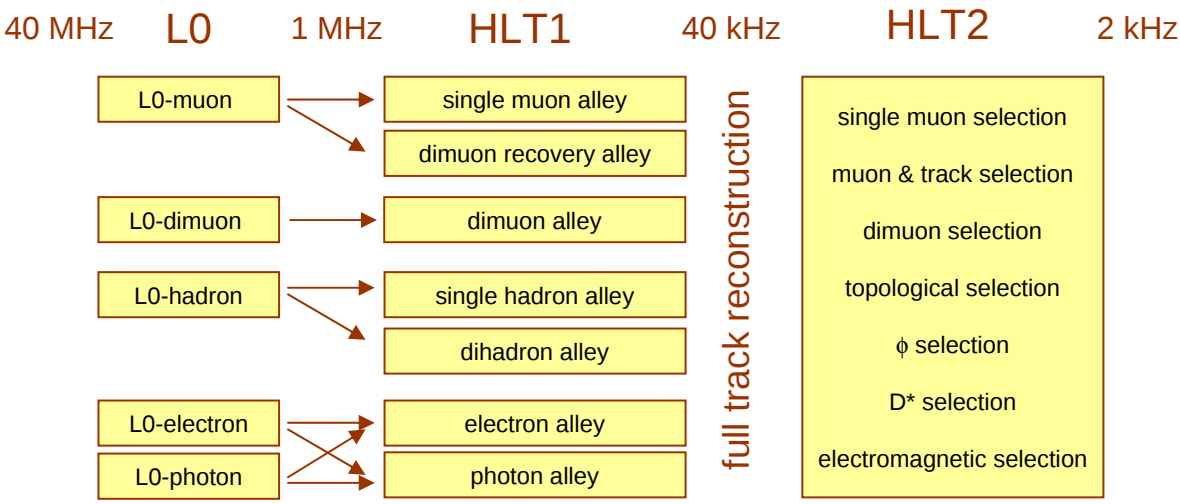

Figure 2.11: Schematic overview of the LHC*b* trigger system [21].

2.5.1 L0 hardware trigger

The L0 trigger uses the specific topology of B events to arrive at a fast trigger decision. Due to the high mass of the B mesons above 5 GeV, the decay products of the B are likely to have a high transverse momentum. L0 therefore triggers on particles with a high transverse momentum in the muon detector or a high transverse energy in the calorimeter. On account of this two L0 decisions exist: the L0 muon and the calorimeter decision. The L0 muon trigger tries to reconstruct muons with a high transverse momentum in the muon chambers, which means that hits on a straight line in the five stations of the muon system are looked for. The track finding algorithms are implemented in custom hardware. For the reconstruction, the track in the muon

stations is extrapolated through the magnetic field with the assumption that the muons originated from the primary vertex. This leads to a transverse momentum resolution of 20% for the L0 muon trigger. The muon tracks with the highest momenta are selected and two selection criteria are applied. The L0 muon trigger requires a candidate with a minimum transverse momentum of 1.3 GeV. The dimuon trigger requires two candidates with $|p_t(1)| + |p_t(2)| > 1.5\,\text{GeV}$. The L0 muon trigger is designed for decays such as $B_s \to J/\psi\phi$.
To come to the L0 calorimeter decision, particles with a high transverse energy deposit in the calorimeter system are searched for. The calorimeter decision is therefore used to trigger charged hadrons, electrons, photons and neutral pions. Information from the ECal and HCal is used to compute the total transverse energy of the particle and from the information of the Preshower and SPD detector a particle hypothesis is established. Of each particle type only the one with the highest E_t is kept. Hadronic candidates are triggered if they have an energy deposit in the calorimeter cluster of more than 3.5 GeV. Electron candidates are triggered in case their transverse energy exceeds 2.6 GeV and for photon candidates a transverse energy of at least 2.3 GeV is required.
Furthermore, a global event veto provides a handle against high multiplicity events and events with several proton-proton collisions. The global event veto uses information of two special Velo sensors located upstream of the nominal interaction point and calorimeter information. An overview of the requirements of the global event veto is shown in table 2.1.

2.5.2 High level software trigger

Online Event Farm

In case of a positive L0 trigger decision, the information from the detector read-out is forwarded to the event filter farm (EFF) via a high speed network with a data throughput of 60 GBytes/s. The event filter farm is planned to consist of 1000 16 core computing nodes that process the L0 triggered events in parallel to facilitate a HLT decision. The total time available for the HLT is restricted by the size of the online event farm: At an input rate of 1 MHz for 16 000 CPUs about 16 ms per event are available on per CPU for the HLT. All CPU times quoted in this thesis are measured on 2.2 GHz 64 bit AMD Opteron processors. Currently, about 35% of the CPUs for the online farm are installed which will be enough for the foreseen physics conditions in the 2009/2010 run. Additional CPUs will be installed if required to obtain the

Table 2.1: Summary of the requirements of the global event veto.

Quantity	Value
Tracks in 2nd vertex	> 3
Pile-Up multiplicity	> 112 hits
SPD multiplicity	> 280 hits
Total ET	> 5 GeV

optimal CPU performance for the given budget. Since the CPU time of the algorithms is heavily dependent on the used CPUs, the timing measurements done in this thesis are conservative. All timing measurements are objected to a relative uncertainty of 20% due to the used CPUs and the type of the simulated test data. A conclusive time measurement will be possible during trigger commissioning at the end of 2009.

First stage of the high level software trigger

The first level of the HLT consists of several algorithm sequences, so called alleys, which are executed depending on the L0 trigger decision. Special care has been taken in the design of the HLT1 alleys that tracks and vertices are reconstructed only once during the execution so as to make sure to not waste CPU time. In the first step of the HLT1, L0 trigger candidates are confirmed taking into account the information of further subdetectors. The main tracking system and the vertex detector are used to gather additional information about the trigger candidates.
Information from the main tracker is supplemented with a regional search for hits in the tracking system. For this purpose, the L0 muon or calorimeter candidates are extrapolated to the trackers assuming that they originate from the interaction region. Then, a track search in the region of interest around the extrapolated track is performed. The regional track reconstruction grants to a short execution time of the algorithms. By this method, the estimate of the transverse momentum is improved to achieve a resolution of about 3%.
The information from the vertex detector is included in two steps. First, the data from the Velo r sensors is used to reconstruct 2D tracks. These 2D tracks are combined with the L0 candidate. In the second step, candidates that seems to be a good match are reconstructed as 3D tracks. The 2D tracks are also used to reconstruct a primary vertex.
If one of the candidates from L0 + Velo or from L0 + Tracker turns out to be a good candidate, the tracks can be updated with the information from the other subdetector to yield a full track in the way described above. In addition to that, a search for a second track can be performed to form, e.g., a dimuon system from a $J/\psi \to \mu\mu$ decay. For track candidates reconstructed as described above, the final trigger decision is taken on the basis of the transverse momentum and the impact parameter of the track or, for HLT1 alleys requiring a second track, also on the p_t and IP of the second track as well as on the distance of closest approach between the two tracks. For a dimuon system, either a minimal impact parameter of 150 μm for each muon and an invariant mass higher than 500 MeV or no minimal IP and an invariant mass of more than 2.5 GeV is required. The latter requirement provides the possibility to obtain a large sample of muons that have no bias in the lifetime distribution for an analysis of the decay $B_s \to J/\psi\phi$.

Second stage of the high level software trigger

In the second stage of the HLT a full event reconstruction as close as possible to the offline reconstruction is performed. The reconstruction is discussed in detail in chapter 4.
After the full reconstruction of all tracks in the event, selections in different trigger lines

are executed in order to choose interesting events. Two different selection approaches are used: inclusive selections, to reconstruct similar decays using the respective event properties, and exclusive selections that are tuned to reconstruct only one specific decay channel. Inclusive selections are more robust against inefficiencies from, e.g., the track reconstruction. Hence, only those selections will be used in the first phase of the LHC running. Currently, inclusive selections for final states containing muons and hadrons are used in the trigger. An inclusive selection for final states with electrons, photons and neutral pions is under development.

The inclusive muon selections consist of three parts: the single muon selection, the dimuon selection and the μ+track selection.
The single muon selection is mainly used for data mining. It requires a track from a secondary vertex with hits in the muon chambers with a high transverse momentum above 3 GeV and an impact parameter greater than 100 μm. It provides a large sample of $B \to \mu X$ decays. Since the opposite side B meson is not used in the trigger, this sample can be used to understand possible biases in the acceptance of events that are introduced by the trigger.
The dimuon selection provides a high efficiency for physics channels such as, e.g., $\mathrm{b} \to \mathrm{J}/\psi\mathrm{X}$, $\mathrm{B_s} \to \mu^+\mu^-$ or $\mathrm{B_d} \to \mathrm{K}^{*0}\mu^+\mu^-$. A dimuon system is triggered either with an invariant mass higher than 3 GeV and a transverse momentum of more than 500 MeV of the individual muons as well as the χ^2 of the dimuon vertex or with an invariant mass above 500 MeV and a requirement on the impact parameter of the both muons. The first possibility, the so called *UnbiasedJPsi* selection, has the advantage that the trigger does not introduce a bias in the lifetime of the triggered B meson.
The μ+track selection provides a robust alternative to the dimuon selection as the second track is not required to have hits in the muon station. This selection demands a transverse momentum above 2 GeV and an impact parameter greater than 50 μm for the muon and the additional track.

The inclusive selections for final states containing hadrons consist of two parts, the topological trigger selections and the inclusive ϕ selections.
The topological trigger selections are designed to trigger $B \to X$ and $D \to X$ decays. The decays are reconstructed subsequently from two, three and four tracks such that a decay can also be reconstructed if a track is missing. The selection is done in two stages. The robust stage selects tracks with a minimal momentum of 2 GeV, a minimal transverse momentum of 300 MeV and an invariant mass larger than 4 GeV (adjusted cuts are used to trigger prompt charm events). Impact parameter cuts as well as geometrical cuts are applied. For events that pass the robust stage, a fast Kalman filter based track fit is used and another selection based on the fitted tracks is performed. A cut on the reduced χ^2 of the track, the separation of the track from the primary vertex and the quality of the secondary vertex are used to reduce the trigger output rate. The benefits of the track fit are discussed in detail in chapter 5.2.
The inclusive ϕ trigger selections are used to select the decay $\phi \to \mathrm{K}^+\mathrm{K}^-$. Since there are about five times as many pions as kaons, a large background from missidentified pions has to be rejected in this selection. Therefore, the information from the RICH detectors is used for particle identification. As the reconstruction of the rings in the

Cherenkov detector is very time consuming, a preselection is used to reduce the rate. At the last stage of the inclusive ϕ trigger, a track fit is applied to further reduce the final output rate.

The total output rate of the LHC*b* trigger system is 2 kHz, which is limited by the bandwidth of the storage system. The selections are tuned to fit within this bandwidth limit. Several scenarios depending on the physics program are prepared for data taking.

Chapter 3

Offline tracking algorithms and tracking performance

3.1 Status of the track reconstruction

The standard offline LHC*b* track reconstruction procedure consists of three steps. In the first step, dedicated algorithms are applied to reconstruct track segments using only the hit information from the vertex detector. In the second step, these track segments are extended by adding T-Station hits. Besides that, a redundant track search is performed by reconstructing track segments in the T-Stations and combining them with Velo seeds.
Afterwards, the parameter estimate of the track is improved using a Kalman filter based fitting approach. Finally, a clone killing algorithm is used to identify and remove duplicated tracks. The tracks found by this approach can be classified as follows (Figure 3.1):

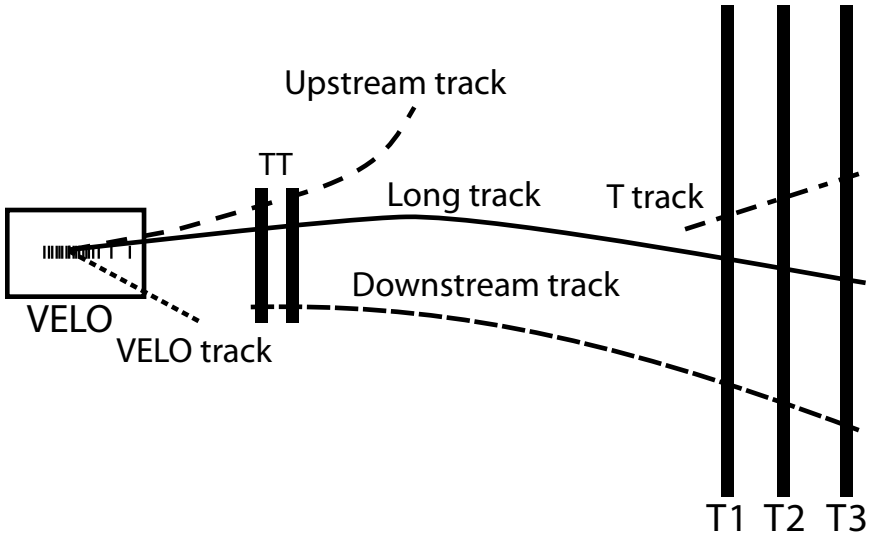

Figure 3.1: Overview of the LHC*b* tracking system and the different track types in the track reconstruction. [14].

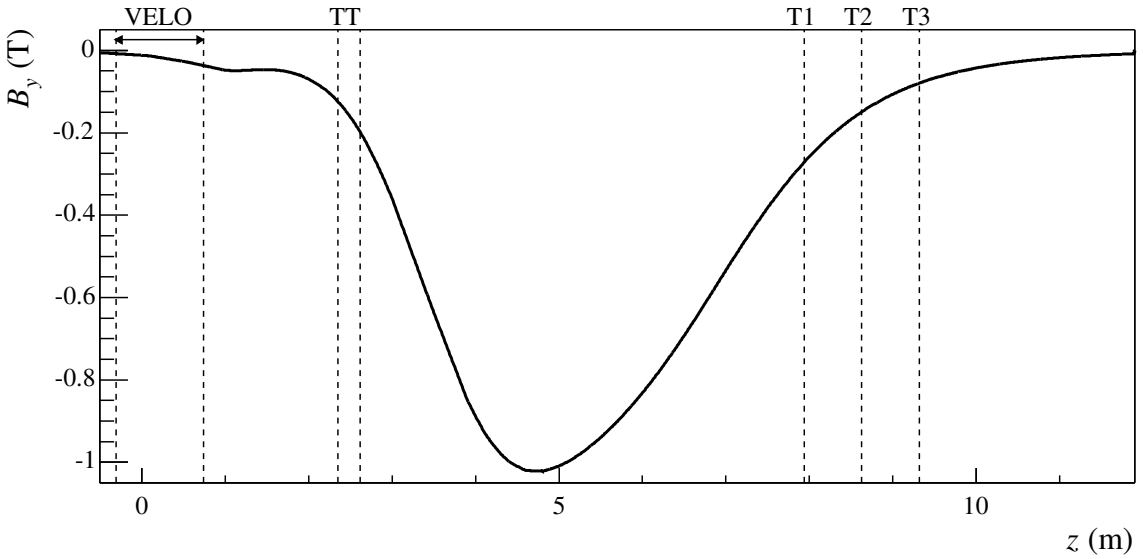

Figure 3.2: B_y component of the magnetic field along the z-axis. Detector components of the tracking system are indicated by dashed lines [14].

- Velo tracks consisting of hits in the vertex detector only.
- Upstream tracks consisting of a Velo track and hits in the trigger tracker only. These are tracks that have a low momentum and potentially are bent out of the detector in the magnetic field.
- Downstream tracks which have hits in the trigger tracker and in the tracking stations. These tracks are usually caused by daughters of long lived neutral particles such as K_s^0 and Λ particles, which decay outside the Velo.
- T-Tracks which are only reconstructed in the T-Stations.
- Long tracks which traverse all the subdetectors of the LHC*b* tracking system. These tracks have the highest quality and are mainly used for physics analysis.

Only tracks reconstructed as long tracks are of interest for the HLT2. Thus I will focus on the description of their reconstruction.

3.1.1 Tracking in the vertex detector

Since the integrated magnetic field in the Velo is sufficiently low (Figure 3.2), the tracks can be described by straight lines in good approximation. The Velo pattern recognition is performed in two steps. First, a 2D reconstruction in the (r-z) projection is done. Secondly, hits from the Velo Φ-Sensors are added to get 3D tracks. The Velo (r-z) and Velo space tracking algorithms are optimized for tracks originating from the beam axis in the Velo. A very high performance for tracks coming from the primary vertex as well as tracks coming from B or D meson decays is achieved, while tracks with random combinations of hits are suppressed. Due to this optimization, the performance becomes

worse for tracks originating from highly displaced vertices.
Thus, a second algorithm, `PatVeloGeneral`, performs a search for displaced tracks originating, e.g., from K_s and Λ decays. The `PatVeloGeneral` algorithm directly uses 3D hits to reconstruct tracks [22]. `PatVeloGeneral` uses only hits that have not been used before by any other reconstruction algorithm because the reconstruction on all hits is very time consuming compared to the standard Velo tracking.
Tracks found by any of the Velo algorithms are used as input for the long track reconstruction.

3.1.2 Track reconstruction using all tracking systems

The standard offline long track reconstruction strategy consists of two redundant algorithms, `PatForward` [23] and the combination of `TsaSeeding` [24] and a matching algorithm.

Forward tracking approach

The forward tracking algorithm starts by using track segments reconstructed by the Velo tracking and extrapolating them through the magnetic field into the T-stations. This is based on the fact that the Velo track segment plus a single hit behind the magnetic field defines the track parameters. A Hough transformation approach is used to pick up further hits in the T-Stations. Finally the track candidates are sorted according to a quality criterion including information about the consistency in y of the Velo seed and the T-Track segment, the χ^2 from an internal fit of the T-Track, and the momentum of the track. Good track candidates are selected and finally TT-Hits are added to those tracks.

T-Station based tracking approach

The seeding approach provides a standalone track reconstruction in the T-Stations. Two algorithms exist for such a T-Station reconstruction: `TsaSeeding` and `PatSeeding`. While the reconstruction principle is similar for both algorithms, there are differences in the implementation which lead to a difference in timing. The offline reconstruction currently uses `TsaSeeding`, thus this algorithm is discussed here. The differences between `TsaSeeding` and `PatSeeding` will be discussed later.
The seeding algorithm starts with two x hits in the first and the last station of the tracking system to predict the position of a possible x hit in the middle. If such a x hit is found, a search window according to a parabolic track hypothesis is opened and a search for additional hits is performed. Due to the magnetic fringe field in the T-Stations, a parabolic track hypothesis has to be used to approximate the track segment in the (x-z) projection. Because of ambiguities from the drift time of the gas detector in total eight track hypotheses have to be tested. The track candidate with the most hits is chosen. Stereo hits are added in an analogous way. However, due to the low fringe field in the (y-z) projection, the tracks can be approximated as straight lines. The selection of the well reconstructed track candidates is performed by calculating a likelihood from the number of observed and expected hits and the χ^2 from a track fit for each track.

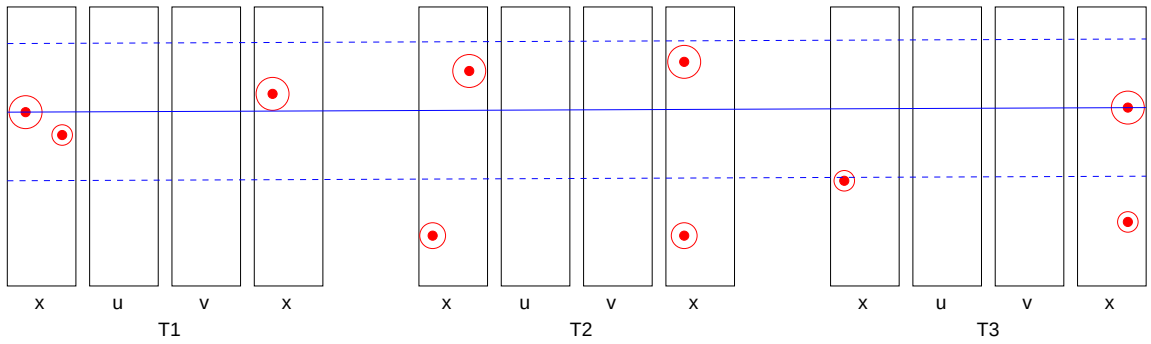

Figure 3.3: First step of T-Station track reconstruction in the (x-z) plane. Two hits in the first and last station are selected, a search window is opened to select a hit in T2 [25].

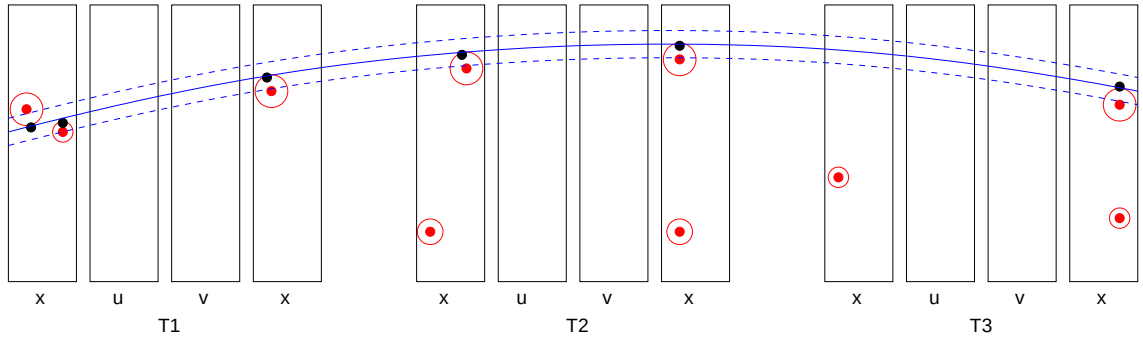

Figure 3.4: Determination of a track hypothesis with a parabola. Additional hits in a search window around the track hypothesis are added to the track. (Figure from [25].)

The calculation of this likelihood is very time consuming, because a full geometrical model of the detector which is needed to predict the number of expected hits. Afterwards, track segments found by `TsaSeeding` are combined with standalone Velo tracks via the `TrackMatching` algorithm. Long track candidates found by the matching algorithm are selected via a quality criterion including mainly information from a track fit. The matching algorithm in addition adds TT hits to the long tracks found.

Each of the two described long track reconstruction strategies provide a high efficiency on Monte Carlo simulated events. However, both strategies reconstruct slightly different subsets of tracks. Therefore, both algorithms are used in the offline reconstruction sequence and doubly reconstructed tracks are removed afterwards 3.2.2.

3.1.3 Offline tracking performance

The aim of the work presented in this thesis is to optimize the online track reconstruction keeping in mind the constraints in timing in HLT2. Ideally, the same reconstruction would be used in HLT2 and offline. In order to compare the HLT2 results to the offline tracking performance, at first the current performance of the offline tracking is reviewed.

A sample of 2000 simulated $B_s \rightarrow D_s\pi$ signal Monte Carlo events is used for this study. The reconstruction has changed since the production of the *Data Challenge 2006* (DC06) Monte Carlo data used in this thesis. Therefore, the tracking is reproduced using `Brunel v35r2` with `REC v7r2`.
A simulated particle is defined as reconstructible as

- Velo track, if there are at least three clusters in both Velo r and ϕ sensors caused by that particle
- T-Station track, if there is at least one x and one stereo cluster in all three T-Stations (T1, T2 and T3).

A particle is reconstructible as long track if it is reconstructible as Velo and as T-Station track. The tracking efficiency $\varepsilon_{\text{rec/all}}$ is defined as

$$\varepsilon_{\text{rec/all}} = \frac{\#\text{ reconstructed} \wedge \text{reconstructible particles}}{\#\text{ reconstructible particles}}\,. \tag{3.1}$$

In Table 3.1 the performance of the track reconstruction procedure for all tracks which are reconstructible as long tracks is listed. Most of the B daughter particles in the LHC*b* experiment have a high momentum of more than 5 GeV. Thus, the tracking efficiency for high momentum tracks is listed separately in the second column of Table 3.1. In the third column, the average fraction of ghost tracks on all reconstructed tracks per event is given. A track is defined as a ghost track, if less than 70% of its hits are consistent with any of the simulated particles.
It can be seen from Table 3.1 that the tracking efficiency for the Velo tracking is very high with a small pollution from misreconstructed tracks. This efficiency degrades in the long track reconstruction. Among the best long tracks, the reconstruction efficiency is about 90.0 % (94.7 % for high momentum tracks) at a ghost rate of 12.8 %. The high rate of misreconstructed tracks is caused by a trade of between the purity of the reconstructed track sample and the efficiency to reconstruct signal tracks. In the offline reconstruction about 75% of the ghost tracks in the final track sample consist of a real Velo track segment and a real T-Station track segment which do not belong to the same MC particle. About 13% of the ghost tracks are caused by a misreconstructed T-Station part and 10% have a ghost track in either the Velo (r-z) or the 3D part of the track. The rest of the ghost tracks is a combination of a ghost Velo track part with a ghost T-Station track.
LHC*b* is a dedicated B physics experiment, thus the reconstruction efficiency for B meson daughter tracks is of particular interest. In table 3.2 the reconstruction efficiency for B meson daughter tracks is listed. It can be seen that the tracking is specifically performant on the reconstruction of B tracks with a efficiency of 92.3% which can be explained by the high momentum of B daughter particles.
In table 3.4 the CPU time consumption of the offline track reconstruction sequence is shown. It shows that the Velo pattern recognition with 5.4 ms uses only a small amount of time in comparison to the long track reconstruction despite its high reconstruction efficiency. The forward tracking takes 27.3 ms. The combination of seeding and matching takes about twice the time of the forward tracking.

Table 3.1: Performance of the different stages of the offline track reconstruction for *all tracks* reconstructible as long tracks. The efficiencies $\varepsilon_{\text{rec/all}}$ quoted are defined with respect to reconstructible Monte Carlo tracks.

reconstruction stage	$\varepsilon_{\text{rec/all}}$	$\varepsilon_{\text{rec/all}}$ for $p > 5\,\text{GeV}$ tracks	ghost rate
Velo (r-z)	98.2%	99.0%	7.1%
Velo 3D	97.3%	98.3%	4.0%
PatForward	85.9%	92.6%	10.5%
TsaSeeding	92.2%	96.1%	6.6%
Matching	82.3%	89.1%	8.0%
Best tracks	90.0%	94.7%	12.8%

Table 3.2: Performance of the different stages of the offline track reconstruction for B *meson daughter tracks* reconstructible as long tracks.

reconstruction stage	$\varepsilon_{\text{rec/B}}$	$\varepsilon_{\text{rec/B}}$ for $p > 5\,\text{GeV}$ tracks
Velo (r-z)	98.3%	99.0%
Velo 3D	97.1%	98.2%
PatForward	89.6%	94.0%
TsaSeeding	94.3%	96.5%
Matching	85.5%	89.9%
Best tracks	92.3%	95.5%

Table 3.3: Performance of the different stages of the offline track reconstruction for K_s *and* Λ *daughter tracks* reconstructible as long tracks.

reconstruction stage	$\varepsilon_{\text{rec/K}_s,\lambda}$	$\varepsilon_{\text{rec/K}_s,\lambda}$ for $p > 5\,\text{GeV}$ tracks
Velo (r-z)	86.3%	89.7%
Velo 3D	91.6%	94.5%
PatForward	77.0%	86.3%
TsaSeeding	90.7%	95.2%
Matching	72.8%	83.8%
Best tracks	81.1%	88.7%

Table 3.4: Timing of the different stages of the offline long track reconstruction. The timing is obtained by running Brunel on one CPU with 1.81 times the speed of 2.8 GHz Xeon.

reconstruction stage	average time per event
Velo (r-z)	0.7 ms
PatVeloSpace	3.0 ms
PatVeloGeneral	1.4 ms
PatForward	27.3 ms
TsaSeeding	47.8 ms
Matching	7.0 ms

3.2 Track parameter estimate and removal of clone tracks

3.2.1 Kalman filter based track fit

A good estimate of the trajectory of a particle is necessary to determine the particle's properties such as its origin vertex in the Velo as well as its momentum from the bending of the track in the magnetic field. In addition to that, the information about the particle hypothesis from the RICH detectors, its energy from the calorimeters and possible hits in the muon system get matched to the particle via its trajectory. To obtain an optimal estimate of the track parameters, a Kalman filter [26, 27] based track fit is used in the LHC*b* experiment.
As long as no multiple scattering is taken into account, the Kalman track fit is mathematically equivalent to a least squares fit. However, it has the advantage of a faster fit procedure, since the prediction of the track is subsequently updated, while new measurements are added to the fit without the need to refit the whole track after the addition of a single hit. Furthermore it provides a rather easy way to account for the deviation in the particles trajectory due to energy loss and multiple scattering on its way through the detector.
The implementation of the track fit used in LHC*b*, which is discussed in [2] and [28], consists of four steps.
First, the fit is initialized with an initial hypothesis of the track which is provided by the pattern recognition. The material budget along the trajectory is calculated to account for possible effects from multiple scattering. Depending on the granularity of the material description, the fit initialization dominates the overall time budget of the fit. For long tracks, the fit starts at the end of the T-Stations, as the application of the track fit in backward direction provides optimal information on the track parameters in the Velo (Figure 3.5).
Then, based on the previous state and covariance, the state of the trajectory from the current to the next measurement is predicted, by fitting the discrepancy to the initial track hypothesis and considering effects from material interaction.
In the filter step the prediction is updated with the information of the next measurement, taking the weighted mean between the predicted track parameters and the information of the measurement. The prediction and the filter steps are repeated until all measurements are added.
To improve the precision of the actual parameters, the above steps are carried out in both positive and negative z direction.
In the offline reconstruction three iterations of the fit in both directions are done to obtain the optimal parameter estimate. Per iteration, the hit with the largest contribution to the χ^2 can be removed. In the next iteration, the track is refitted without this outlier. After all three iterations, a maximum of two outliers is removed.
The full offline fitting procedure as described above takes on average 130 ms per event.

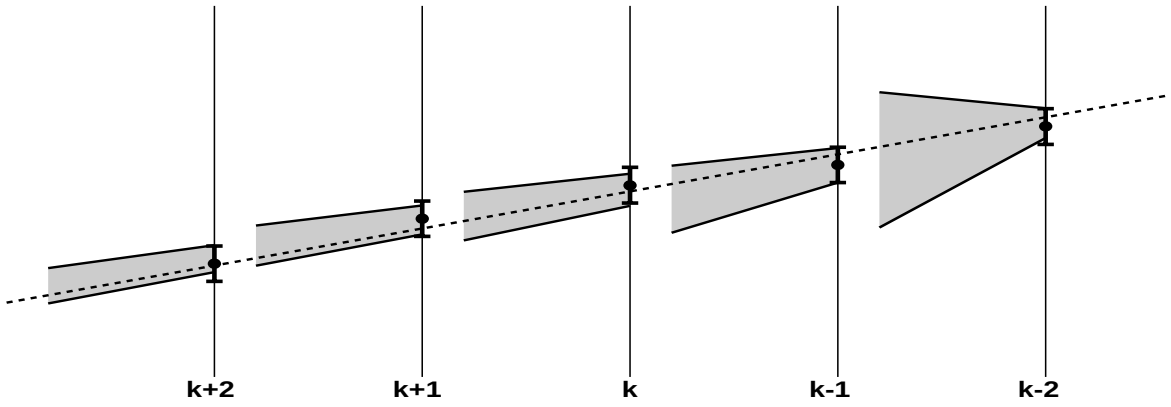

Figure 3.5: Principle of the Kalman filter track fit: The vertical lines correspond to the detector planes with measurements and their errors. The cones indicate the increasing uncertainties due to multiple scattering effects. With each subsequent step, this uncertainty gets smaller due to the additional information [28].

3.2.2 Clone track identification

As discussed in chapter 3.1.2 two redundant approaches for the reconstruction of long tracks are used in the offline pattern recognition: the forward tracking and a seeding/matching strategy. Both approaches reconstruct more than 80% of the Monte Carlo reconstructible tracks, so that a large number of tracks is found twice by the forward and the match tracking.
If two tracks share more than 70% of their hits they are treated as clone tracks. To identify such tracks, a clone killing algorithm is used after the track fit [29]. This clone killer decides on the basis of the number of hits and the χ^2 from the track fit which track of an identified clone pair is kept. Ideally, only one track per particle is kept. After the clone killer, the fraction of clone tracks among all real long tracks is 1.6%.

Chapter 4

Online track reconstruction sequence

In this Chapter, the differences between the offline track reconstruction and the track reconstruction in the second stage of the high level software trigger are examined. The impact of several pattern recognition algorithms added to the HLT2 reconstruction sequence on the tracking efficiency, the ghost rate and the CPU time is discussed. This Chapter concludes with a discussion of possible changes to the offline tracking sequence to make the tracking in the trigger and offline more consistent.

4.1 The standard reconstruction sequence in the final stage of the software trigger (HLT2)

As mentioned in Chapter 3.1.3, the HLT2 tracking is on purpose very similar to the offline track reconstruction, which has been discussed in 3.1. Ideally, there should be no difference between the online and the offline track reconstruction. However, since only a limited time budget is available on the trigger, a full reconstruction as it is done offline is not feasible. In order to understand the differences in the final track sample, the similarities and differences between the two tracking approaches are discussed in this section.

4.1.1 Tracking in the vertex detector

The Velo tracking in HLT2 starts with the Velo 2D track reconstruction in the (r-z) plane. Afterwards, Velo 3D tracks are reconstructed. Up to this point, the Velo track reconstruction is identical to the offline reconstruction. However, `PatVeloGeneral` for the reconstruction of Velo tracks from highly displaced vertices is not run in the original HLT2 reconstruction. As discussed in 3.1.1, this leads to a decrease of the tracking performance especially for particles with long decay lengths, such as the K_s and the Λ.

4.1.2 Track reconstruction using all tracking systems

The online long track reconstruction is done solely by the `PatForward` algorithm. Due to timing constraints, the redundant approach to reconstruct long tracks in the forward direction and with a T-Station seeding approach is abandoned in the standard HLT2 reconstruction. `PatForward` uses the same procedure as in the offline case with the only difference that TT hits are not added at the end of `PatForward` in HLT2. This leads to a slightly degraded momentum resolution for fitted tracks. In addition to that, the inclusion of TT hits in the offline forward tracking provides a useful input for the quality of the reconstructed track candidates and can therefore suppress misreconstructed tracks in the offline forward tracking. As a result, the ghost rate is higher in the online reconstruction.

4.1.3 Track parameter estimate and vertex fit

In the offline track reconstruction, a Kalman filter track fit is used to obtain a high quality parameter estimate of the reconstructed tracks. This parameter estimate affects on the one hand the quality of reconstructed physics parameters such as the momentum and the mass of the particles and on the other hand it gives a handle to suppress poorly reconstructed tracks via the track quality estimate χ^2. The time for using this full Kalman track fit is not available on HLT2.
Offline, the primary vertex is fitted using fitted Velo 3D and long tracks. On HLT2 in contrast, the primary vertex is per default reconstructed from unfitted Velo 2D tracks, which leads to a significantly reduced vertex resolution. Improvements in the vertex reconstruction and the application of a track fit in HLT2 will be discussed in Chapter 5.

4.1.4 Tracking performance of the default HLT2 reconstruction sequence

In Figure 4.1 a schematic comparison between the offline and the HLT2 reconstruction sequence is shown. The reconstruction efficiency of the online reconstruction with respect to the offline reconstruction for all tracks is given in Table 4.1. The reconstruction efficiency $\varepsilon_{\text{trig/all}}$ in the HLT2 context is defined as

$$\varepsilon_{\text{trig/all}} = \frac{\#\text{ tracks reconstructed on HLT2 and offline}}{\#\text{ tracks reconstructed offline}}\,. \tag{4.1}$$

This definition provides a very convenient measure to compare the two different tracking approaches as it allows direct access to the additional loss in efficiency introduced due to the different tracking strategies. The tracking efficiencies for `PatForward` are related to all offline reconstructed long tracks, including tracks found by the offline matching. Table 4.1 shows that for Velo 2D tracks, for which the same reconstruction is used as in the offline case, the efficiency with respect to the offline reconstruction is 100%. This is no longer true for the Velo 3D reconstruction due to the fact that `PatVeloGeneral` is not used in HLT2. Comparing the Velo 3D efficiency with respect to offline for B daughter and K_s/Λ tracks, it can be seen that this has little effect on the B meson reconstruction, but a significant impact on K_s/Λ (Table 4.2).

About 93.0% of the long tracks available in the offline long track collection are reconstructed in HLT2. The difference to the offline reconstruction is a combination of the missing Velo seeds from `PatVeloGeneral` that are not prolonged to forward tracks and the missing T-Station seed tracks from `TsaSeeding` that are combined to long tracks with the matching algorithm offline. This in particular is a problem for the B reconstruction. Depending on the decay mode, two to six tracks are required to fully reconstruct a B meson. If only 94.8% of the B daughter tracks are found this leads to a B meson reconstruction efficiency with respect to offline of just 70% to 89%.
The ghost fraction of 11.4% for forward tracks is about 1% higher than offline because of the missing TT hits in the forward tracking.

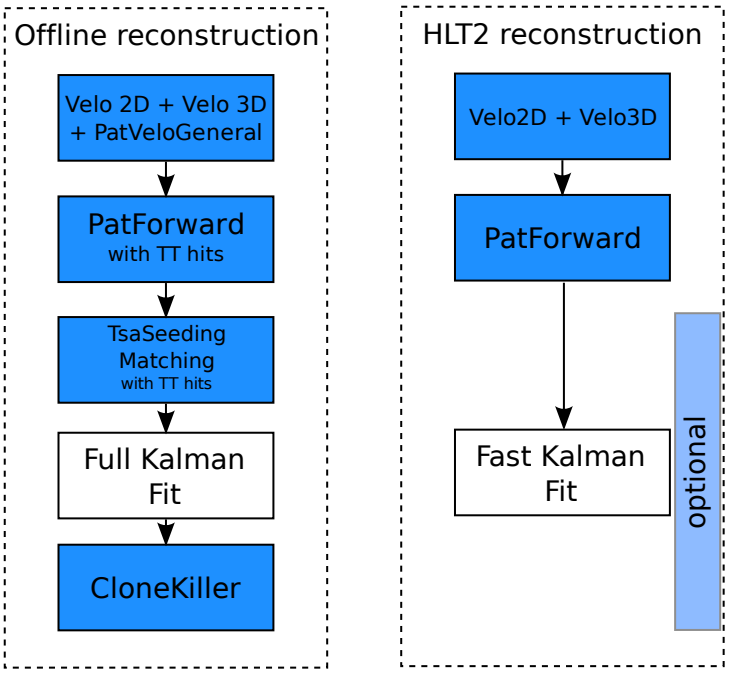

Figure 4.1: Schematic comparison between the default offline and the HLT2 long track reconstruction sequence.

Table 4.1: Performance of the different stages of the online track reconstruction for *all tracks* reconstructible as long tracks. The efficiencies $\varepsilon_{\text{trig/all}}$ quoted are defined relative to the offline reconstructed tracks.

reconstruction stage	$\varepsilon_{\text{trig/all}}$	$\varepsilon_{\text{trig/all}}$ for $p > 5\,\text{GeV}$ tracks	ghost rate
Velo (r-z)	100.0%	100.0%	7.2%
Velo 3D	94.5%	99.0%	3.7%
PatForward	93.0%	95.8%	11.4%

Table 4.2: Performance of the different stages of the online track reconstruction for *B meson* and K_s/Λ daughter tracks reconstructible as long tracks. The efficiencies quoted are defined with respect to offline reconstructed tracks.

reconstruction stage	$\varepsilon_{\mathrm{trig/B}}$	$\varepsilon_{\mathrm{trig/B}}$ for $p > 5\,\mathrm{GeV}$ tracks	$\varepsilon_{\mathrm{trig/K_s,\lambda}}$
Velo (r-z)	100.0%	100.0%	100%
Velo 3D	97.6%	99.4%	81.3%
PatForward	94.8%	96.2%	82.3%

Table 4.3: Timing of the different stages of the online long track reconstruction. The timing is obtained by running DaVinci on one CPU with 1.81 times the speed of 2.8 GHz Xeon.

reconstruction stage	average time per Event
Velo (r-z)	0.1 ms
PatVeloSpace	3.0 ms
PatForward	28.3 ms

4.1.5 HLT2 signal efficiency and minimum bias rate

Besides the performance of the track reconstruction algorithms, another benchmark of the trigger performance is the trigger efficiency of signal events as well as the final trigger output rate. These two quantities depend not only on the tracking performance but also on the performance of the trigger selections. Since the selections used in HLT2 are still under development [30], no work has been done yet to retune the actual selections. The effect of the improved tracking performance on the final output rate and on the signal efficiency is shown where applicable without retuning the selections. To estimate the signal efficiency of the HLT2 trigger selections, a sample of 2000 offline selected events of each of the decays $\mathrm{B_s} \to \mathrm{D_s^-}\pi^+$, $\mathrm{B_d} \to \pi^+\pi^-$, $\mathrm{B_s} \to \mathrm{J}/\psi\phi$ and $\mathrm{B}^+ \to \mathrm{D}^0(\mathrm{K_S^0}\pi^+\pi^-)\mathrm{K}^+$ was used. These signal samples were selected out of the LHC*b* key physics channels because they represent a broad spectrum of requirements for the HLT. The samples were reproduced from standard DC06 signal samples with the same version of the reconstruction software as the one used on the trigger and were stripped with the standard offline selections. This procedure is identical to the one used to produce the standard trigger benchmark datasets, which are used to tune the trigger selections. The only difference is the usage of consistent versions of the reconstruction algorithms. Because of the high efficiency of the pattern recognition algorithms, an inconsistency between the offline and the online reconstruction will always result in a loss in efficiency. Thus, the usage of consistent algorithm versions is mandatory. The quoted efficiency $\varepsilon_{\mathrm{HLT2}}$ is defined as

$$\varepsilon_{\mathrm{HLT2}} = \frac{\#\text{ events selected on L0} \wedge \text{HLT1} \wedge \text{HLT2} \wedge \text{offline}}{\#\text{ events selected on L0} \wedge \text{HLT1} \wedge \text{offline}}\,. \tag{4.2}$$

This definition is particularly useful to measure trigger efficiencies, because it grants direct access to the inefficiencies introduced by the second stage of the high level software trigger.

Table 4.4: Summary of the default HLT2 signal efficiency. Given are the overall HLT2 efficiencies for the specific signal sample as well as the efficiency and the name of the two most efficient selections *on HLT1 accepted events*. $\varepsilon_{\text{HLT2}}$ is the OR of all HLT2 selections.

Signal sample	$\varepsilon_{\text{HLT2}}$	best selection	2nd selection
$B_d \to \pi^+\pi^-$	89%	B2HH: 78%	TopoTF2BodyReq2Yes: 70%
$B_s \to D_s^-\pi^+$	91%	TopoTF4BodyReq4Yes: 78%	TopoTF4BodyReq3Yes: 77%
$B_s \to J/\psi\phi$	98%	UnbiasedJPsi: 95%	BiasedDiMuonMass: 78%
$B^+ \to D^0(K_S^0\pi^+\pi^-)K^+$	71%	TopoTF3BodyReq3Yes: 43%	TopoTF3BodyReq4Yes: 40%

Table 4.5: Summary of the default HLT2 minimum bias rate. Given is the overall HLT2 minimum bias rate, as well as the rate for the five most contributing selections. Hlt2Global is the OR of all selections.

Selection	minimum bias rate
Hlt2Global	4070 Hz
Hlt2TopoTF4BodyReq4Yes	1150 Hz
Hlt2TopoTF3BodyCharmSignal	1030 Hz
Hlt2SingleMuon	890 Hz
Hlt2TopoTF4BodyReq3Yes	800 Hz
Hlt2TopoTF3BodyReq4Yes	620 Hz

Where the signal efficiency on individual HLT2 selections is quoted, the condition *selected by any HLT2 selection* is replaced by, e.g., *triggered by Hlt2UnbiasedJPsi selection*. With this definition one has direct access to inefficiencies introduced by single HLT2 selections.
For the determination of the final trigger output a sample of roughly 91 000 L0xHLT1 accepted minimum bias events was used. This number of events corresponds to 2.48 seconds of LHC run time at an luminosity of $2\,\text{fb}^{-1}$. These events have been stripped from a total of 9.1 million minimum bias events, which is the total amount available in DC06 data by using the HLT1 bandwidth division [31]. These minimum bias events contain simulated proton proton collisions at a center of mass energy of 14 TeV. No further assumptions have been made for the generation of these events.

In table 4.4 the total HLT2 signal efficiency $\varepsilon_{\text{HLT2}}$ for the four selected benchmark channels, as well as the efficiencies for the most efficient selections[1] are given. It can be seen that the efficiency for the decay $B_s \to J/\psi\phi$ is by far the highest out of the four samples and that this decay is mostly triggered by the lifetime unbiased J/ψ selection [21]. The reason for this is that the dimuon system from the J/ψ decay has a very clean

[1]The selection names given in the table are the technical identifiers from the trigger software. B2HH refers to the exclusive $B \to hh$ selection. TopoTF2BodyReq2Yes, TopoTF3BodyReq3Yes, TopoTF3BodyReq4Yes, TopoTF4BodyReq3Yes and TopoTF4BodyReq4Yes refer to the inclusive topological two, three and four body selection in the post track fit stage. UnbiasedJPsi and BiasedDiMuonMass refer to the lifetime unbiased (i.e. without impact parameter cut) and to the lifetime biased inclusive dimuon selections. For a detailed description of the HLT2 trigger selections, see Chapter 2.5.2

signal. In comparison to that the hadronic two body decay $B_d \rightarrow \pi^+\pi^-$ and the four body decay $B_s \rightarrow D_s^-\pi^+$ exhibit a rather poor selection efficiency of only 89% - 91%. This is caused by the difference in tracking efficiency and parameter estimate of the track fit with respect to the offline tracking. Further inefficiencies are introduced by the application of a different set of cuts in the HLT2 and in the offline selections. The performance of the four body hadronic decay $B^+ \rightarrow D^0(K_S^0\pi^+\pi^-)K^+$ is even worse than those of the aforementioned ones because of the subsequent decay $D_0 \rightarrow K_s\pi\pi$. Due to the long lifetime of the K_s mesons about 54% of them decay outside of the Velo and can only be reconstructed as Downstream or T-Tracks. Since there is no standalone reconstruction of T-Tracks in the default configuration of the HLT2 tracking, those K_s tracks are missing and consequently the decay is not reconstructible. A potential profit of the K_s reconstruction from the standalone T-Track reconstruction in HLT2 will be discussed in Chapter 4.4.
In Table 4.5 the global minimum bias rate after HLT2 as well as the rate of the five most contributing selections is shown. As one can see, the total rate of about 4 kHz is way above the aim of 2 kHz final trigger rate. The highest contribution to the global rate comes from the topological trigger selections. As these selections trigger B hadrons in an inclusive approach via their specific event topology, they are in particular sensible to misreconstructed tracks and to combinatorics.
It should be noted that the development of the HLT2 is still in progress and that efforts are on the way to reach the design output rate of 2 kHz. The HLT2 selections are currently retuned to attain this goal [30]. Other options such as improvements in the track reconstruction and the suppression of the rate contributions from misreconstructed tracks are discussed later in this thesis.

4.2 Extension of the tracking in the vertex detector

As discussed in Chapter 4.1.1 the HLT2 Velo pattern recognition is identical with the one used offline besides the `PatVeloGeneral` algorithm. The algorithm itself reconstructs Velo tracks emerging from highly displaced vertices such as K_s and Λ daughter tracks (see also Chapter 3.1.1). `PatVeloGeneral` only uses clusters in the Velo that have not previously been used by the Velo space tracking.
When adding `PatVeloGeneral` to the HLT2 track reconstruction sequence, the performance of the Velo tracking improves to the same level as offline (Table 4.6). Because `PatVeloGeneral` finds additional Velo seed tracks which can be used by the forward tracking to find long tracks, the performance of the forward tracking improves by an average of 0.5% for all long tracks. The main improvement is about 8.9% for K_s and Λ daughter tracks. The remaining difference in the tracking efficiency for long tracks is caused by the fact that only the forward tracking is used in HLT2 to reconstruct these tracks.
The selection efficiency for the signal samples also profits from the increase in tracking efficiency (Table 4.9) and is raised by 1%.
The introduction of the `PatVeloGeneral` tracking in the HLT2 tracking sequence enhances the minimum bias rate by 50 Hz (1%) and thus has a negligible contribution to the overall trigger rate (Table 4.14). The contribution to the overall HLT2 tracking

Table 4.6: Performance of the different stages of the online track reconstruction with PatVeloGeneral for *all tracks* reconstructible as long tracks. The efficiencies $\varepsilon_{\text{trig/all}}$ quoted are defined with respect to offline reconstructed tracks.

reconstruction stage	$\varepsilon_{\text{trig/all}}$	$\varepsilon_{\text{trig/all}}$ for $p > 5\,\text{GeV}$ tracks	ghost rate
Velo (r-z)	100.0%	100.0%	7.1%
Velo 3D	100.0%	100.0%	4.1%
PatForward	93.5%	96.5%	11.4%

Table 4.7: Performance of the different stages of the online track reconstruction with PatVeloGeneral for *B meson* and K_s/Λ daughter tracks that are reconstructible as long tracks. All efficiencies quoted are defined with respect to the offline reconstructed tracks.

reconstruction stage	$\varepsilon_{\text{trig/B}}$	$\varepsilon_{\text{trig/B}}$ for $p > 5\,\text{GeV}$ tracks	$\varepsilon_{\text{trig/K}_s,\lambda}$
Velo (r-z)	100.0%	100.0%	100%
Velo 3D	100.0%	100.0%	100%
PatForward	95.2%	96.5%	92.7%

timing of 1.1 ms is only 5% of the online reconstruction and therefore also negligible (Table 4.8). `PatVeloGeneral` will be used per default in the HLT2 reconstruction.
The reason for the still poor trigger efficiency in the $B^+ \to D^0(K^0_S\pi^+\pi^-)K^+$ channel is the generally poor long track reconstruction efficiency for K_s tracks (Table 4.9). Only about 46% of the K_s's from B's decay in the acceptance region of the Velo. Since the K_s itself is a neutral particle and does not leave hits in the Velo, only daughters from K_s's, which decay in the Velo, can be reconstructed as long tracks and used in the trigger, while offline also Downstream tracks are available for K_s reconstruction. At the moment, no Downstream tracks are used on the trigger. Since the Downstream tracking takes about 3 ms an inclusion in the HLT2 tracking may be affordable in the future. However, this requires in addition to make use of a T-Station seeding algorithm.

Table 4.8: Timing of the different stages of the online long track reconstruction including PatVeloGeneral. The timing is obtained by running DaVinci on one CPU with 1.81 times the speed of 2.8 GHz Xeon.

reconstruction stage	average time per Event
Velo (r-z)	0.1 ms
PatVeloSpace	3.0 ms
PatVeloGeneral	1.1 ms
PatForward	28.3 ms

Table 4.9: Summary of the HLT2 signal efficiency including PatVeloGeneral. Given is the overall HLT2 efficiency for the specific signal sample as well as the efficiency and the name of the three most efficient selections *on HLT1 accepted events*. $\varepsilon_{\mathrm{HLT2}}$ is the OR of all HLT2 selections.

Signal sample	$\varepsilon_{\mathrm{HLT2}}$	best selection	2nd selection
$B_d \to \pi^+\pi^-$	90%	B2HH: 79%	TopoTF2BodyReq2Yes: 71%
$B_s \to D_s^-\pi^+$	91%	TopoTF4BodyReq4Yes: 78%	TopoTF4BodyReq3Yes: 77%
$B_s \to J/\psi\phi$	98%	UnbiasedJPsi: 95%	BiasedDiMuonMass: 79%
$B^+ \to D^0(K_S^0\pi^+\pi^-)K^+$	72%	TopoTF3BodyReq3Yes: 44%	TopoTF3BodyReq4Yes: 41%

Table 4.10: Summary of the HLT2 minimum bias rate with PatVeloGeneral. Given is the overall HLT2 minimum bias rate as well as the rate for the five most contributing selections. Hlt2Global is the OR of all selections.

Selection	minimum bias rate
Hlt2Global	4120 Hz
Hlt2TopoTF4BodyReq4Yes	1190 Hz
Hlt2TopoTF3BodyCharmSignal	1040 Hz
Hlt2SingleMuon	890 Hz
Hlt2TopoTF4BodyReq3Yes	840 Hz
Hlt2TopoTF3BodyReq4Yes	640 Hz

4.3 Addition of information from the Trigger Tracker to the tracks

In the offline reconstruction hits from the trigger tracker are added to long tracks at the end of the forward tracking (see Chapter 3.1.2). Adding TT hits to long tracks improves the momentum resolution of fitted long tracks from $\Delta p/p = 0.6\%$ to $\Delta p/p = 0.46\%$, as shown in Figure 4.2.
In HLT2, trigger tracker hits are not adjoint per default to long tracks. Historically this was justified in terms of timing and robustness of the pattern recognition algorithms. Since those facts do no longer hold, TT hits will now be used in the forward tracking. This leads to a 5% increase in timing to the forward tracking, which is affordable.
The `PatForward` [23] algorithm uses TT hits in the selection of the track candidates. A significant amount of the ghost tracks produced in the forward tracking is caused by a wrong extrapolation of the Velo seed track through the magnetic field. While the Velo seed, as well as the T-Station part of the track are real track segments, the combination of both results in a ghost track. Due to the high efficiency of the silicon strip detector of the trigger tracker it is very likely that a real track has hits in this sub detector while a ghost track does not. At the end of `PatForward` a search for ghost tracks and clone tracks is performed. In case such misreconstructed tracks are found the algorithm decides which tracks to keep on the basis of the respective hits in the T-Stations and the TT. The addition of TT hits to the track thus gives an good handle to suppress misreconstructed tracks in the forward tracking.

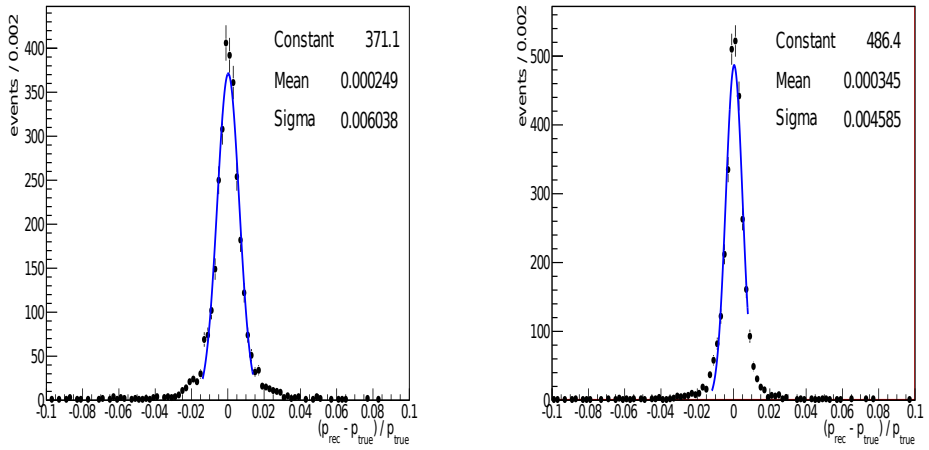

(a) fitted long tracks without TT hits (b) fitted long tracks with TT hits

Figure 4.2: Effect of TT hits on forward tracks. Momentum resolution of the fitted long tracks without TT hits (a). Improvement in the momentum resolution of the fitted long tracks with TT hits (b).

The inclusion of TT hits in long tracks brings the minimum bias rate down from 4120 Hz to 3810 Hz. The tracking performance, as well as the efficiency of signal events stays the same, the ghost fraction on long tracks decreases from 11.4% to 10.5% to the same as offline.
As a result of the studies done in the course of this thesis, TT hits are adjoint to the HLT2 long tracks both in the forward and the match tracking.

4.4 T-Station based track reconstruction

The biggest difference between the track reconstruction sequence offline and in HLT2 lies in the reconstruction of long tracks. As discussed in Chapter 4.1.2, only the forward tracking approach is used in HLT2. Due to this fact not more than 93.0% of the offline long tracks and 94.8% of the offline B tracks are reconstructed in the trigger. To optimize this efficiency, a redundant T-Station based tracking approach was introduced to the HLT2 reconstruction in the course of this thesis.
Most of the long track candidates are already reconstructed by the `PatForward` algorithm. The T-Station hits of these long tracks are not used in the T-Station seeding to reduce the timing. Thus, mainly track segments from T-Tracks or Downstream tracks are reconstructed by the seeding algorithm and only few T-Track segments from long tracks are recovered. Those tracks are combined with all reconstructed Velo seeds by the matching and good matches are selected as long tracks.
As discussed in Chapter 3.1.2, the offline tracking with `TsaSeeding` together with the offline matching takes about 64 ms. With `PatSeeding` [32], another seeding algorithm with a similar approach as `TsaSeeding` exists and provides the possibility to perform a search for T-Tracks only on those hits that have not been used previously. The principle of the pattern recognition in `PatSeeding` is the same as discussed in Chapter 3.1.2, but

Table 4.11: Timing of the different stages of the online long track reconstruction including PatSeeding and PatMatch. The timing is obtained by running DaVinci on one CPU with 1.81 times the speed of 2.8 GHz Xeon.

reconstruction stage	average time per Event
Velo (r-z)	0.1 ms
PatVeloSpace	3.0 ms
PatVeloGeneral	1.1 ms
PatForward	28.3 ms
PatSeeding	20.2 ms
PatMatch	1.2 ms

the algorithm uses a different method to choose good track candidates. Furthermore, a Hough Transformation approach is used by `PatSeeding` in the reconstruction of 3D tracks, which is faster than the simple straight line approach performed in `TsaSeeding`. The search for complicated track candidates such as tracks migrating from IT to OT is done in a second step after the normal track search. This results in a significantly reduced execution time for `PatSeeding`.
Furthermore, `PatMatching` as matching algorithm has the advantage of not relying on the information from the track fit and is optimized to have a fast execution time. This configuration of the seeding/matching approach on the trigger takes 21.4 ms which is two thirds of the time used for the forward tracking and may under certain conditions be affordable on the trigger (Table 4.11).
The efficiency of the matching algorithm for long tracks is 4.5% with a ghost rate of 65.9% (Table 4.12). The significantly higher ghost fraction and the lower efficiency compared to `PatForward` are caused by the fact that the backward tracking takes only unused hits and only complicated tracks are left for the reconstruction after the forward tracking. `PatForward` reconstructs on average 31.5 long tracks per event correctly while the seeding/matching approach recovers only 2.2 (Figures 4.3 (a)). Figure 4.3 (b) shows that the large ghost fraction of the matching also affects the ghost fraction of all HLT2 long tracks (*HLT2Long*) and increases it from 10.5% to 20.1%. As discussed below, this severely affects the final trigger output rate in HLT2.

The efficiency of the HLT2 long track reconstruction for all long tracks as well as for B, K_s and Λ daughters can be found in tables 4.12 and 4.13. The results shown include the aforementioned changes to the online tracking.
When using the seeding/matching in the HLT2 reconstruction, the efficiency with respect to offline reconstructed tracks rises from 93.5% to 98.0% for all long tracks. The improvement for B tracks is 2.8% leading to a reconstruction efficiency of 98.8% for all B tracks. For K_s and Λ daughters the efficiency rises by 4.9% to 97.6%.

The 10% higher ghost rate in the HLT2 long tracks increases the final HLT2 output rate by 20% from 3810 Hz to 4560 Hz.
The increase in the track reconstruction efficiency has a positive impact on the signal efficiency of the HLT2 selections. The HLT2 global efficiency $\varepsilon_{\mathrm{HLT2}}$ improves by about 1% for the decay channels $\mathrm{B_s} \to \mathrm{D_s^-}\pi^+$ $\mathrm{B_d} \to \pi^+\pi^-$ and $\mathrm{B_s} \to \mathrm{J}/\psi\phi$ and 2% for $\mathrm{B}^+ \to \mathrm{D}^0(\mathrm{K_S^0}\pi^+\pi^-)\mathrm{K}^+$.

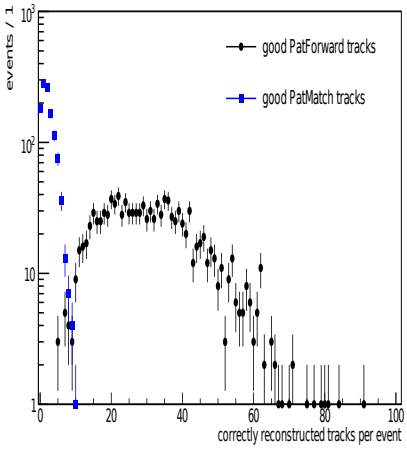

(a) Correctly reconstructed tracks per event

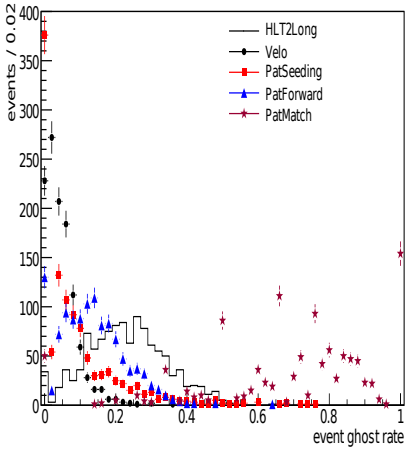

(b) Event ghost fraction

Figure 4.3: Performance overview of the HLT2 T-Station seeding and the track matching: (a) Number of correctly reconstructed long tracks in HLT2. (b) Event ghost fraction for all stages of the HLT2 pattern recognition.

Table 4.12: Performance of the different stages of the online track reconstruction for *all tracks* that are reconstructible as long tracks including PatSeeding and PatMatch. The efficiencies $\varepsilon_{\text{trig/all}}$ quoted are defined with respect to the offline reconstructed tracks.

reconstruction stage	$\varepsilon_{\text{trig/all}}$	$\varepsilon_{\text{trig/all}}$ for $p > 5\,\text{GeV}$ tracks	ghost rate
PatForward	93.5%	96.2%	10.5%
PatSeeding	10.2%	5.0%	7.4%
PatMatch	4.5%	2.4%	65.9%
HLT2Long	98.0%	98.5%	20.1%

Because the three and four body hadronic B meson decays suffer the most from inefficiencies introduced by the tracking, the increase is with 2% to 3% particularly high for the three and the four body topological triggers (for a detailed discussion of the different trigger selection see Chapter 2.5.2).

However, the large increase in the final trigger output rate makes this scenario not feasible for usage in HLT2.

In the approach presented so far, all hits that have not been used previously are used to form T-Station segments . These segments are then combined with all reconstructed Velo track segments, irrespectively if the Velo segment has been used before.

One possible measure to lower the ghost rate from the matching, is to run the `PatMatching` algorithm not on all Velo seeds but only on such tracks that have not been used by `PatForward` or produced only a poor forward track.

When using only Velo seeds that have not produced a long track in the forward tracking, the tracking efficiency of all long tracks drops from 98.0% to 97.5% (Table 4.16). The efficiency of B daughter tracks decreases by about 0.4% to 98.4% on all tracks. Since less Velo seeds are now used to produce a long track, less misreconstructed tracks

Table 4.13: Performance of the different stages of the online track reconstruction including PatSeeding and PatMatch for *B meson* and K_s/Λ daughter tracks that are reconstructible as long tracks. The efficiencies quoted are defined with respect to the offline reconstructed tracks.

reconstruction stage	$\varepsilon_{\mathrm{trig/B}}$	$\varepsilon_{\mathrm{trig/B}}$ for $p > 5\,\mathrm{GeV}$ tracks	$\varepsilon_{\mathrm{trig/K_s,\lambda}}$
PatForward	95.2%	96.5%	92.7
PatSeeding	7.3%	4.0%	19.1
PatMatch	3.7%	2.6%	5.0
HLT2Long	98.8%	99.0%	97.6

Table 4.14: Summary of the default HLT2 minimum bias rate including PatSeeding and PatMatch. Given are the overall HLT2 minimum bias rate, as well as the rates for the five most contributing selections. Hlt2Global is the OR of all selections.

Selection	minimum bias rate
Hlt2Global	4560 Hz
Hlt2TopoTF4BodyReq4Yes	1310 Hz
Hlt2TopoTF3BodyCharmSignal	1120 Hz
Hlt2SingleMuon	940 Hz
Hlt2TopoTF4BodyReq3Yes	940 Hz
Hlt2TopoTF3BodyReq4Yes	690 Hz

are produced, too, and the ghost fraction drops from 20.1% to 14.1%. This also has an impact on the minimum bias rate, which decreases by about 10% from 4560 Hz to 4120 Hz (Table 4.17). This is about 8% higher than the 3810 Hz in a scenario with `PatVeloGeneral` and the addition of TT hits to long tracks but has an increased tracking and selection efficiency.
To regain some of the loss in trigger efficiency one may not veto all Velo seeds that produced a forward track, but only the ones which produced a good forward track. This would require a track quality variable such as the χ^2 from the track fit which is not available on that stage of HLT2.
There is no significant reduction of the signal efficiency visible that is caused by the decrease in tracking efficiency besides a 1% loss in the decay $\mathrm{B}^+ \to \mathrm{D}^0(\mathrm{K}^0_\mathrm{S}\pi^+\pi^-)\mathrm{K}^+$.

Table 4.15: Summary of the default HLT2 signal efficiency including PatSeeding and PatMatch. Given is the overall HLT2 efficiency for the specific signal sample as well as the efficiency and name of the three most efficient selections *on HLT1 accepted events*. $\varepsilon_{\mathrm{HLT2}}$ is the OR of all HLT2 selections.

Signal sample	$\varepsilon_{\mathrm{HLT2}}$	best selection	2nd selection
$\mathrm{B_d} \to \pi^+\pi^-$	91%	B2HH: 79%	TopoTF2BodyReq2Yes: 73%
$\mathrm{B_s} \to \mathrm{D_s^-}\pi^+$	92%	TopoTF4BodyReq4Yes: 80%	TopoTF4BodyReq3Yes: 79%
$\mathrm{B_s} \to \mathrm{J}/\psi\phi$	99%	UnbiasedJPsi: 95%	BiasedDiMuonMass: 79%
$\mathrm{B}^+ \to \mathrm{D}^0(\mathrm{K}^0_\mathrm{S}\pi^+\pi^-)\mathrm{K}^+$	74%	TopoTF3BodyReq3Yes: 44%	TopoTF3BodyReq4Yes: 42%

The signal efficiency remains unchanged for the other decay channels (see table 4.18).

Table 4.16: Performance of the online long track reconstruction with PatSeeding and PatMatch on unused Velo seeds. The efficiencies $\varepsilon_{\text{trig/all}}$ quoted are defined with respect to offline reconstructed tracks. The event average ghost fraction is 14.1%.

	$\varepsilon_{\text{trig}}$	$\varepsilon_{\text{trig}}$ for $p > 5\,\text{GeV}$ tracks
all long tracks	97.5%	98.1%
B daughter long tracks	98.4%	98.7%
K_s/Λ daughter long tracks	97.4%	98.8%

Table 4.17: Summary of the default HLT2 minimum bias rate including PatSeeding and PatMatch on unused Velo seeds. Given is the overall HLT2 minimum bias rate as well as the rate for the five most contributing selections. Hlt2Global is the OR of all selections.

Selection	minimum bias rate
Hlt2Global	4120 Hz
Hlt2TopoTF4BodyReq4Yes	1090 Hz
Hlt2TopoTF3BodyCharmSignal	970 Hz
Hlt2SingleMuon	910 Hz
Hlt2TopoTF4BodyReq3Yes	780 Hz
Hlt2TopoTF3BodyReq4Yes	600 Hz

Table 4.18: Summary of the default HLT2 signal efficiency including PatSeeding and PatMatch on unused Velo seeds. Given is the overall HLT2 efficiency for the specific signal sample as well as the efficiency and name of the three most efficient selections *on HLT1 accepted events*. $\varepsilon_{\text{HLT2}}$ is the OR of all HLT2 selections.

Signal sample	$\varepsilon_{\text{HLT2}}$	best selection	2nd selection
$B_d \to \pi^+\pi^-$	91%	B2HH: 79%	TopoTF2BodyReq2Yes: 73%
$B_s \to D_s^-\pi^+$	92%	TopoTF4BodyReq4Yes: 80%	TopoTF4BodyReq3Yes: 79%
$B_s \to J/\psi\phi$	99%	UnbiasedJPsi: 95%	BiasedDiMuonMass: 79%
$B^+ \to D^0(K_S^0\pi^+\pi^-)K^+$	73%	TopoTF3BodyReq3Yes: 44%	TopoTF3BodyReq4Yes: 41%

With the presented tuning, the introduction of the redundant seeding/matching long track reconstruction is feasible in HLT2. The overall tracking efficiency for all long tracks increases by 4%, and the selection efficiency, depending on the selection, by up to 3%. The final trigger output rate is increased by 8% with respect to a scenario without the T-Station based track reconstruction. The additional algorithms need about two thirds of the time of the forward tracking. It has to be tested on data if this fits within the timing conditions of the trigger.

4.5 Potential improvement to the offline tracking

The online reconstruction efficiency with respect to the offline efficiency amounts to 98% after the inclusion of all optimizations presented in this chapter. The remaining 2% difference to a full agreement of 100% are caused by the following differences to the offline tracking:

- Different seeding algorithms are used offline (`TsaSeeding`) and on the trigger (PatSeeding).
- Offline the seeding is performed on all T-Station hits, but on the trigger the seeding runs only on unused hits.
- A different matching algorithm is applied offline (`TrackMatching`) and on the trigger (`PatMatching`).

To prove that a more consistent use of tracking algorithms is possible without any loss in efficiency in the offline reconstruction, a scenario with `PatSeeding` run on all hits in the offline reconstruction is compared to `PatSeeding` run on unused hits in the online reconstruction.
In Table 4.19 the offline tracking efficiency with `PatSeeding` applied on all hits as offline seeding algorithm is presented. When comparing this to the numbers obtained with `TsaSeeding` in the offline reconstruction as shown in Tables 3.1 - 3.3, one can see that the usage of `PatSeeding` in the offline reconstruction provides an ghost fraction of 12.6% which is 0.2% lower than with `TsaSeeding`. Furthermore, `PatSeeding` is about 1% more efficient on all long tracks and 0.5% on high momentum tracks. The effects on B daughter tracks and K_s/Λ tracks are of the same order of magnitude. The running of `PatSeeding` takes 31 ms, while `TsaSeeding` takes 56 ms. From these numbers, it can be concluded that the offline tracking with `PatSeeding` would not have less performance as it has with `TsaSeeding`.

If one compares the impact of the consistent use of the two tracking algorithms on the agreement of the online and the offline tracking, one finds that they agree better. The online tracking efficiency, which was defined as a measure for the agreement of the online and the offline tracking, increases by about 0.2% for all long tracks and B daughters, being now very close to 100%. The remaining difference can be explained by the different matching algorithm and by the fact that the seeding on the trigger is run on unused hits only.
If the seeding is run on unused hits offline and the same matching algorithm is used offline and on the trigger, a complete agreement of the two tracking strategies can be achieved.

Table 4.19: Performance of offline long track reconstruction with PatSeeding. The efficiencies $\varepsilon_{\text{track}}$ quoted are defined with respect to MC reconstructible tracks. The event average ghost fraction is 12.6%.

	$\varepsilon_{\text{track}}$	$\varepsilon_{\text{track}}$ for $p > 5\,\text{GeV}$ tracks
all long tracks	91.1%	95.2%
B daughter long tracks	93.1%	96.1%
K_s/Λ daughter long tracks	82.1%	90.0%

Table 4.20: Performance of online long track reconstruction with PatSeeding offline and online. The efficiencies $\varepsilon_{\text{trig}}$ quoted are defined with respect to offline reconstructed long tracks. The event average ghost fraction is 20.1%.

	$\varepsilon_{\text{trig}}$	$\varepsilon_{\text{trig}}$ for $p > 5\,\text{GeV}$ tracks
all long tracks	98.2%	99.0%
B daughter long tracks	99.0%	99.4%
K_s/Λ daughter long tracks	97.0%	98.0%

Chapter 5

Online vertex fit and track parameter estimate

5.1 3D primary vertex reconstruction for the High Level Software trigger

The primary vertex of an event is a very important information for the physics analysis as well as for the trigger. All selection criteria utilizing the long B meson lifetime need to calculate the distance of a track or secondary vertex from the primary vertex. In general, the primary vertex is calculated from all tracks in the Velo and all long tracks. In the offline reconstruction the primary vertices are calculated using 3D Velo seeds and long tracks. To ensure an optimal parameter estimate, all tracks are fitted with the full Kalman track fit. In the trigger only 2D Velo tracks are used to determine the position of the primary vertex. The used Velo seeds are not fitted.
The reason for applying the 2D vertex reconstruction is that in HLT1 the vertexing algorithm has very tight timing constraints and the full track search is performed only for (r-z) tracks. In HLT2, however, a full event reconstruction very similar to the one used offline, is performed. For the HLT2 all Velo 3D tracks are available. The remaining difference to the offline tracking is that they are not fitted.
The use of the 3D vertex algorithm takes about 2 ms, which is well within the time budget of HLT2.

Figure 5.1 compares the primary vertex resolution in the x, y and z coordinates for the offline 3D vertex and the HLT2 2D and 3D vertex. One can see that the

Table 5.1: Summary of the primary vertex resolution for different PV reconstruction scenarios.

reconstruction scenario	σ_x	σ_y	σ_z
HLT2 2D	20.6 μm	20.6 μm	60.1 μm
HLT2 3D	11.1 μm	10.9 μm	48.4 μm
Offline 3D	8.5 μm	8.5 μm	40.7 μm

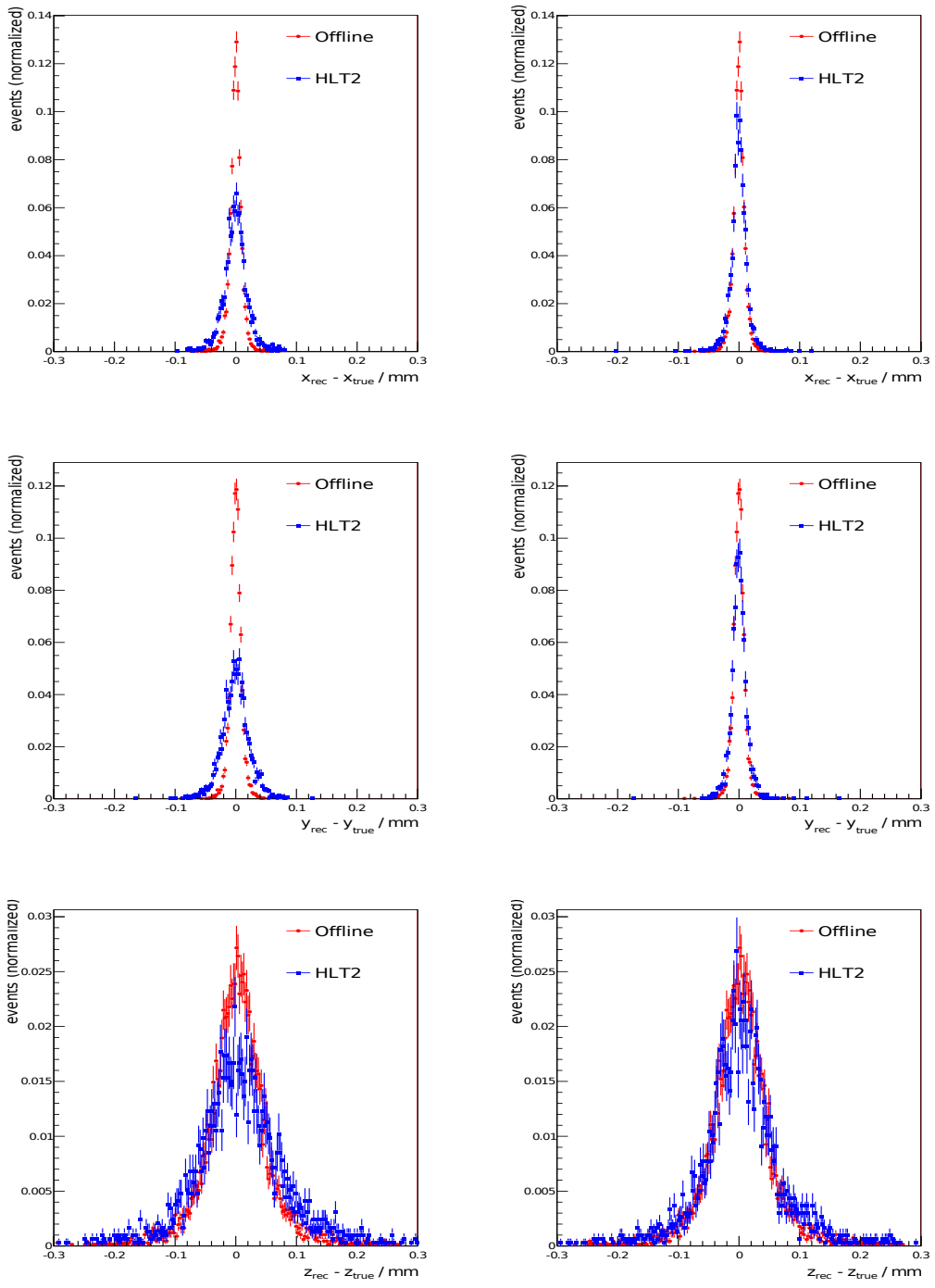

Figure 5.1: 2D (left, blue) and 3D (right, blue) HLT2 primary vertex resolution. To allow a comparison, the offline PV resolution is also plotted (red). One can be see that the 2D primary vertex resolution in the trigger is significantly worse than offline, while the situation improves for the 3D primary vertex.

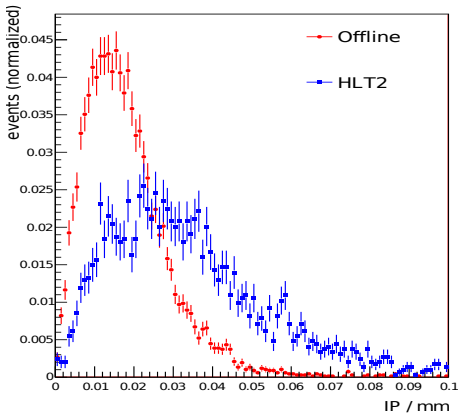

(a) HLT2 with 2D PV

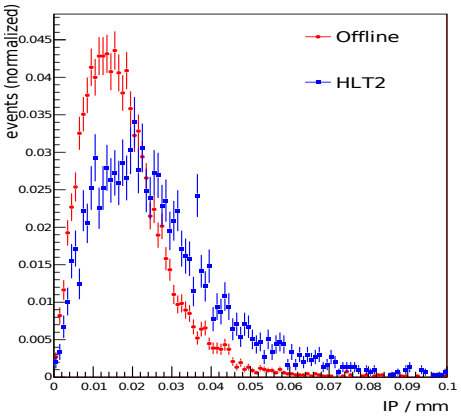

(b) HLT2 with 3D PV

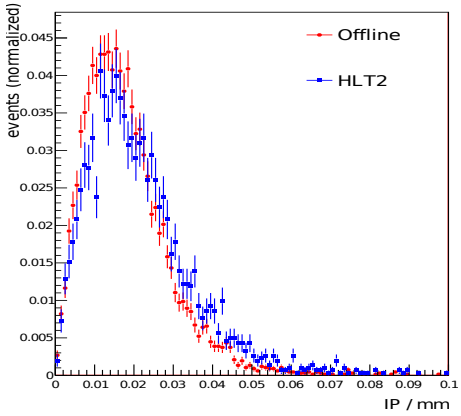

(c) HLT2 with the fast track fit and 3D PV

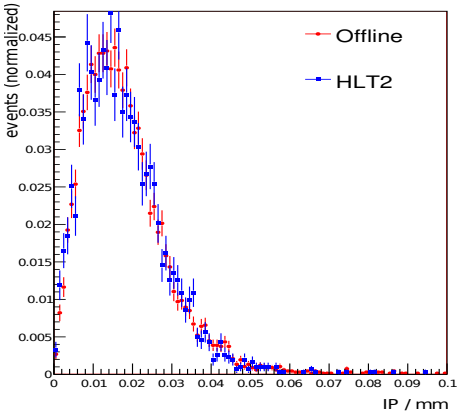

(d) HLT2 with the fast track fit and offline PV.

Figure 5.2: HLT2 impact parameter of B mesons with respect to the primary vertex for the decay $B_d \to \pi^+\pi^-$. Comparison of IP with standard HLT2 and 2D PV (a) and standard offline and HLT2 with 3D vertex (b). Influence of the track fit on IP resolution (c) and comparison of the offline full track fit and the HLT2 fast track fit with same PV (d).

HLT2 distribution, tough significantly broader for the 2D vertex, approaches the offline performance when the 3D vertex is used. The x and y coordinates have almost a four times better resolution compared to the z coordinate due to the design of the Velo sensors (see Chapter 2.1.1). In Table 5.1 the resolution for the three scenarios is compared. The resolution is defined as the width of a Gaussian fitted to the distributions shown in Figure 5.1.

Most of the hadronic selections in the HLT2 cut on an impact parameter between 50 μm and 100 μm to distinguish tracks from the primary vertex from tracks coming from B decays. The impact parameter of a track is defined as the distance of closest approach of the track to the primary vertex. Ideally, for tracks coming from the primary vertex, this distance should be zero, while for tracks from displaced vertices it should be

greater than zero. However, the impact parameter has only a finite resolution owing to the following matters: the quality of the track parameter estimate and the resolution of the primary vertex. This leads to a impact parameter distribution with a non zero mean even for prompt particles. Since the applied impact parameter cuts are of the same order of magnitude as the primary vertex resolution, this effect can not be neglected. The effect of a different primary vertex reconstruction scenario on the impact parameter distribution of the B meson from the decay $\mathrm{B_d} \to \pi^+\pi^-$ is shown in Figure 5.2. It shows that the HLT2 impact parameter distribution in Figure 5.2 (a) is smeared out in comparison to the offline distribution when a 2D primary vertex reconstruction is applied in the trigger. If a 3D vertex is used to determine the impact parameter, the HLT2 distribution already approaches the offline distribution (Figure 5.2 (b)).
As it has been said, the usage of the 3D vertex also improves the separation power between prompt background tracks and signal tracks. The rate of minimum bias events which pass the HLT2 final selection improves by 6% from 3810 Hz to 3570 Hz, while the signal efficiency is found to stay unchanged. In case the seeding is used, the minimum bias rate decreases by 11% from 4520 Hz to 4020 Hz and by 6% from 4120 Hz to 3870 Hz with the optimized seeding and matching approach. A further background suppression might be achieved by retuning the impact parameter based cuts made in the HLT2 selections. The 3D vertex reconstruction will be used from now on in HLT2.

5.2 Fast Track Fit for the High Level Software Trigger

Besides a good pattern recognition a precise estimate of the track parameters is necessary for both the signal selection as well as for the physics analysis. In the trigger the reconstruction algorithms have to satisfy severe timing constraints. Therefore the full Kalman filter track fit can not be used in the trigger.
In HLT1, a simplified version of the Kalman filter approach is applied on specific trigger candidates at a reasonable low rate [21]. In comparison to the offline fit as described in Chapter 3.2.1, the fast version that is used in the trigger is simplified in two ways.
In the prediction of the trajectory from one measurement to the next, the fitter takes into account the material distribution within the detector to correctly describe multiple scattering. These material description is derived from a database for each step. Depending on the granularity of this description this process takes a significant amount of time. The fast fit therefore uses a much coarser material description and does not describe multiple scattering effects as optimal as the offline fit, but saves a factor of three in CPU time.
To further reduce the CPU time, the fast version of the fit uses only one unidirectional iteration starting with a measurement in the T-Stations and extending the tracks through the detector. This is sufficient in most cases because it provides an optimal estimate of the trajectory in the Velo. Without more iterations, there is no outlier removal possible. Moreover, the usage of a unidirectional fit starting in the T-Stations can impose a problem if, e.g., the matching of a track to a calorimeter cluster is needed in the trigger due to the large track uncertainties at this point of the detector. A bidirectional fit can be used in such cases.

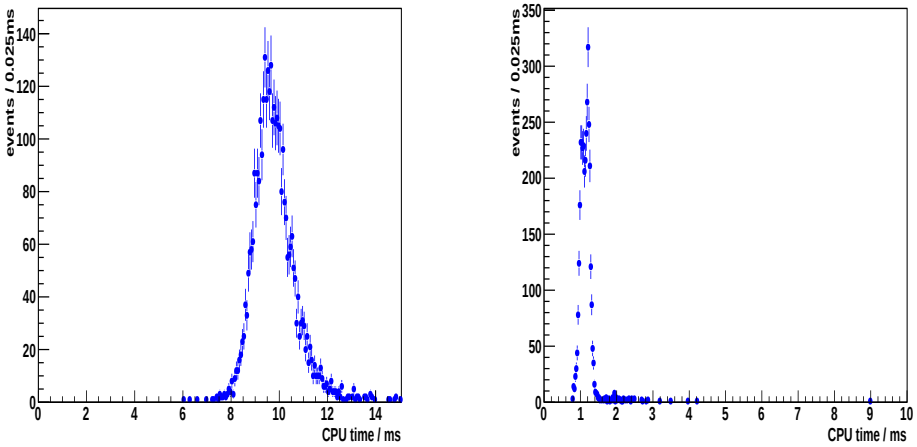

(a) CPU time for the full Kalman fit

(b) CPU time for the simplified Kalman fit

Figure 5.3: CPU time per track for the Kalman fit in HLT2: The full fit (a) takes on average 10 ms per track, while the simplified fit (b) takes on average 1 ms per track.

Figure 5.3 shows the average time used per track in the fit. The full Kalman base fit takes about 10 ms per track, which is mainly used for the lookup of the material. The fast version with a simplified material description takes about 1 ms per track.

The fast track fit improves both the determination of the track momentum and the spatial resolution, as well as the error on these quantities. It furthermore provides an estimate of the track quality via the χ^2 of the fit.

5.2.1 Momentum and mass estimate

One of the quantities enhanced by the track fit is the momentum resolution. Figure 5.4 (a) shows the relative momentum resolution of unfitted HLT2 long tracks. The width of the distribution obtained from fitting a Gaussian is $\Delta p/p = 1\%$. Figure 5.4 (c) shows the improvement from the fast track fit. The momentum resolution has now refined to $\Delta p/p = 0.5\%$ and is close to the offline resolution, which is slightly below $\Delta p/p = 0.5\%$. The enhancement in the momentum resolution is important for HLT2, because the invariant mass of B mesons and of intermediate resonances provides a good trigger signature.

The improvement in the momentum determination is directly visible in the invariant mass resolution. Figure 5.4 (b) shows the invariant mass distribution for $B_d \to \pi^+\pi^-$on HLT2 without a track fit. The width of the mass peak is 48 MeV. This improves together with the track fit by a factor of two to a width of 24 MeV which is also close to the offline mass resolution of 21 MeV. This enables a tightening of the mass windows, while retaining the same amount of sidebands that are needed for the physics analyses.

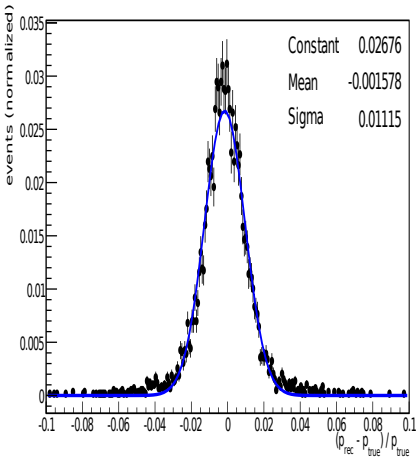

(a) Default HLT2 momentum resolution

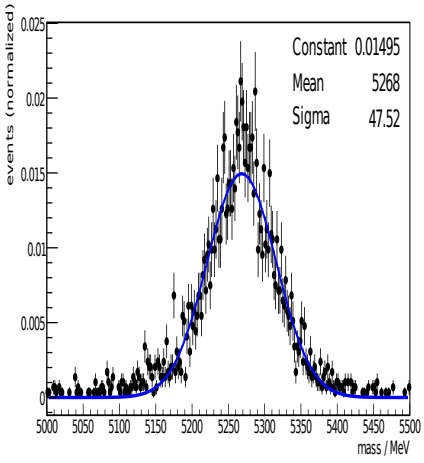

(b) Default HLT2 mass resolution

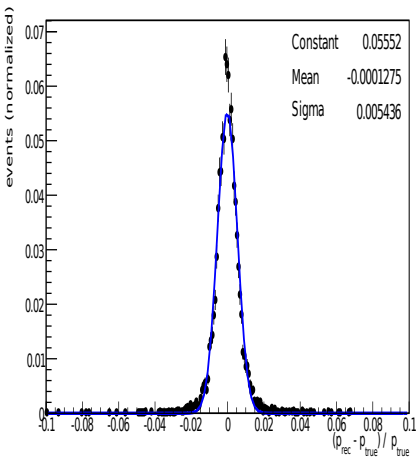

(c) HLT2 momentum resolution with fast fit

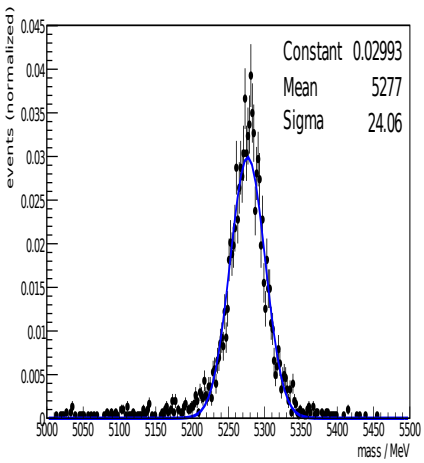

(d) HLT2 mass resolution with fast fit

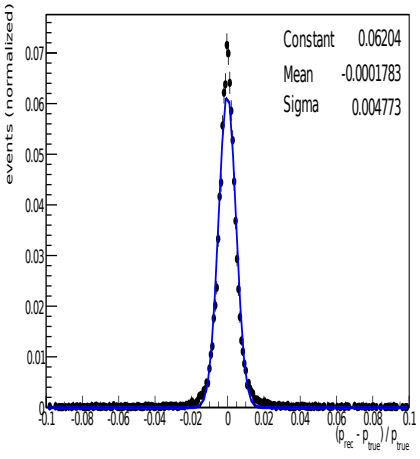

(e) Offline momentum resolution with full fit

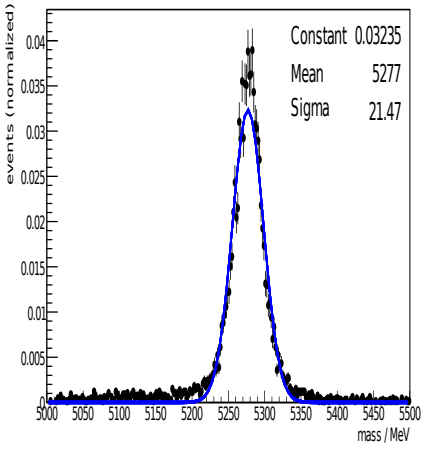

(f) Offline mass resolution with full fit

Figure 5.4: HLT2 momentum and mass resolution. Comparison of momentum resolution for particles reconstructed in the standard HLT2 (a), with simplified Kalman fit (c) and with full offline fit (c). In addition, the mass resolution of the B^0 mass for the different reconstruction scenarios is shown (right side). The simplified Kalman fit reaches almost the performance of the full offline fit.

5.2.2 Impact parameter estimate

The impact parameter resolution in HLT2 was already discussed in Chapter 5.1. As it was said before, the impact parameter resolution depends on two factors: the resolution of the primary vertex and the accuracy of the track estimate. Figure 5.2 (b) shows that there is a remaining difference between the impact parameter distribution of B mesons in HLT2 and offline when the HLT2 3D vertex is used. In Figure 5.2 (c) in addition a track fit is used to fit all long tracks. The improved track parameter estimate leads to a better agreement between the two distributions. Since the 3D vertex on HLT2 is still slightly worse than offline, there remains a difference between the online and the offline case. In Figure 5.2 (d) this difference vanishes, because the same vertex is used for the impact parameter determination in the trigger and offline.
Since a wrongly determined impact parameter on the trigger is specifically important in case the particle came from the primary vertex, those tracks are studied separately. In Figure 5.5 (a) the offline and the HLT2 impact parameter distribution for fitted tracks with a true impact parameter smaller than $50\,\mu$m are shown. Due to the fact that the primary vertex resolution is of the same order of magnitude in the trigger, those tracks can be considered as coming from the primary vertex. As one can see, there is no difference between the two distributions. A bias of either the offline or the online fit to higher impact parameters is expected to shift the according distribution to higher impact parameters. In Figure 5.5 (b) the difference between the offline impact parameter estimate and the one on the trigger is shown for real tracks. If there was a bias the distribution would be shifted in either direction. Since there is no such shift visible, it can be concluded that the difference of the fast online fit and the full offline fit has no measurable effect on the impact parameter determination in the trigger. The limiting factor in the impact parameter determination in the trigger is the primary vertex resolution.

5.2.3 Track quality estimate

One of the advantages of the fast fit in HLT2 is the estimate of the track quality obtained via the reduced χ^2 of the fit. In Figure 5.6 the reduced χ^2 distribution for real tracks as well as for ghost tracks is shown. One can see that a large fraction of the real tracks have a rather small reduced χ^2 around one, while the misreconstructed tracks tend to have a higher reduced χ^2. Thus by cutting on the reduced χ^2, a large fraction of ghost tracks can be suppressed, while retaining the signal efficiency at more than 99%. The reduced χ^2 is used, e.g., in the topological trigger selection to reduce the trigger rate of misreconstructed tracks.

In HLT2 no track fit was used per default on the trigger. In this thesis, the effect of the improved parameter estimate and the usage of track quality estimates of the fit in order to suppress misreconstructed tracks as well as the timing in HLT2 was studied. On account of this studies, the fast track fit is used in the topological trigger selections and the inclusive ϕ trigger (see Chapter 2.5.2).

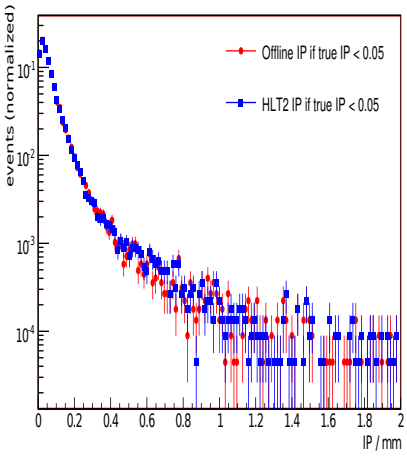

(a) IP for prompt stable particles

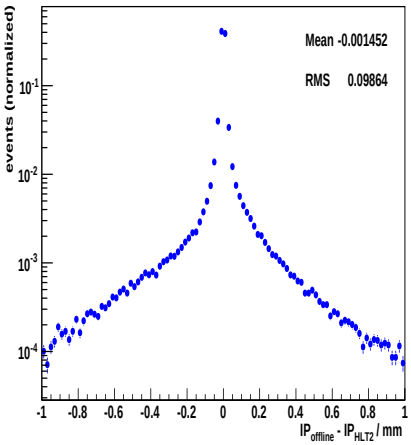

(b) Online and offline IP difference for prompt stable particles

Figure 5.5: Comparison of the online and offline impact parameter determination for prompt particles. Impact parameter distribution for offline and HLT2 tracks that have a true IP smaller than 50 μm (a). Difference between the offline and the online impact parameter of real tracks (b).

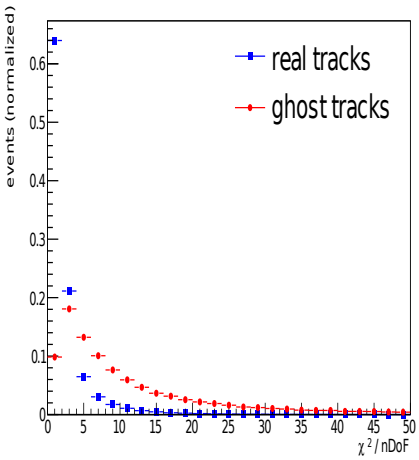

Figure 5.6: Reduced χ^2 distribution of the fast fit for true and misreconstructed tracks (ghosts).

Chapter 6

Misreconstructed tracks in the high level software trigger

In this chapter, the composition of events falsely accepted by the final trigger selection in HLT2 is discussed. The impact of misreconstructed tracks on this background is discussed and methods to identify them are studied.

6.1 Analysis of events accepted by the final trigger selection

The cross section for $c\bar{c}$ $\sigma_{c\bar{c}} = 3.8\,\text{mb}$ and $b\bar{b}$ $\sigma_{b\bar{b}} = 0.7\,\text{mb}$ production are two orders of magnitude below the total cross section at $\sqrt{s} = 14\,\text{TeV}$ of $\sigma_{tot} = 100\,\text{mb}$. The software trigger has the task to bring down the event rate by a factor of 500. Only a small fraction of the accepted events constitute interesting physics signal events. Understanding the origin of the remaining minimum bias background which does not represent signal events is crucial to be able to improve the performance of the high level software trigger. Depending on the reconstruction scenario, the final HLT2 output rate as presented in the last chapters is between 3570 Hz and 4020 Hz. This is about twice as much as the HLT2 design criterion of 2000 Hz.

6.1.1 Background composition

In order to study the background composition after the final HLT2 selection, a sample of 91 000 minimum bias events which are both L0 and HLT1 accepted is used. This sample corresponds to 2.48 s of data taking at the nominal running conditions. These events are reconstructed with the HLT2 reconstruction sequence as discussed in Chapter 4 including the improved Velo tracking. Information from the trigger tracker is used in the long track reconstruction and a 3D primary vertex reconstruction is performed. This scenario has an output rate of 3570 Hz in HLT2. The composition of the minimum bias rate is monitored with a standard LHC*b* tool [33], which analyses those candidates of each selection that fired the trigger and sorts them into different categories:

- **Signal and quasi signal:** All final state particles reconstructed by the HLT2 selection are associated to a simulated particle and come from the decay required

Table 6.1: Composition of HLT2 trigger candidates averaged over all selections. Candidates containing at least one ghost track are responsible for two thirds of the trigger rate.

background category	rate	fraction
Signal and quasi signal	92.8 Hz	2.6%
Physics and low mass	139.2 Hz	3.9%
Reflection	7.1 Hz	0.2%
Pileup	25.0 Hz	0.7%
Prompt	214.2 Hz	6.0%
$b\bar{b}$, $c\bar{c}$ and light flavour	100.0 Hz	2.8%
Ghost	2449.0 Hz	68.6%
Uncategorized	546.0 Hz	15.3%

by the selection. For quasi signal the intermediate resonances in the decay chain can be missing.

- **Physics background and low mass background:** All final state particles are correctly reconstructed and associated to a simulated particle, but are not coming from the required decay or are falsely associated to the required decay, due to some missing final state particles. This could be for example a true $B_s \to K^+K^-$ reconstructed as $B^0 \to K^+K^-$ and true $B_s \to \pi^+\pi^-\pi^0$ reconstructed as $B^0 \to \pi^+\pi^-$.
- **Reflection background:** All particles are correctly matched to a simulated particle but at least one particle has a wrong mass hypothesis, e.g. a K^+ is misidentified as a π^+. The particles originated from a similar decay than the required one, e.g. a true $B^0 \to \pi^+\pi^-$ that is reconstructed as $B_s \to \pi^+K^-$.
- **Pileup:** The final state particles which are used to form the trigger candidate originated from different collisions. The other final state particles are not ghosts.
- **Prompt:** At least one of the final state particles which are used to form the trigger candidate originates directly from the primary vertex. The other final state particles are not ghosts.
- **$\mathbf{b\bar{b}}$, $\mathbf{c\bar{c}}$:** At least one of the final state particle comes from a $b\bar{b}$ or $c\bar{c}$ quark pair. The other final state particles are neither ghosts nor prompt particles.
- **Ghost background:** At least one of the final state particles was a misreconstructed track.
- **Misidentified muons:** Tracks falsely identified as muon tracks in the single muon trigger lines that were non-ghosts in the tracking system.

In Table 6.1 the contribution of the different background categories to the overall HLT2 output rate is listed. The most important contribution comes from trigger candidates that contain at least one misreconstructed track. Such candidates are responsible for 68.61% or 2449 Hz of the total output rate of 3570 Hz.

Table 6.2: Origin of long tracks classified as ghosts in the pattern recognition for offline and online reconstructed tracks and ghost from triggered HLT2 candidates. One can see that the fraction of ghosts with a Velo (r-z) or 3D ghost part is higher in the sample of those ghost tracks that passed the topological trigger selections.

ghost origin	offline reconstruction	online reconstruction	triggered ghost tracks
Mismatched parts	74.5%	48.1%	38.4%
Velo (r-z)	1.0%	0.9%	1.1%
Velo 3D	6.9%	11.5%	22.3%
Velo (r-z) and 3D	2.5%	5.6%	9.3%
T-Station	12.4%	25.4%	22.1%
Velo (r-z) and T-Station	0%	0.4%	0.4%
Velo 3D and T-Station	1.2%	3.3%	3.3%
Velo (r-z), 3D and T-Station	1.5%	4.6%	3.1%

6.1.2 The origin of misreconstructed tracks

For an effective treatment of trigger candidates with misreconstructed tracks it is necessary to understand the origin of the misreconstructed tracks in the pattern recognition. While the overall criterion to distinguish a good track from a ghost track is that at least 70% of the hits on the track have to originate from the same simulated particle there are several possibilities why a track can be a ghost track. A track is a

- **Velo** (r-z) ghost if less than 70% of the Velo (r-z) hits originate from the same simulated particle.
- **Velo 3D ghost** if less than 70% of the Velo hits originate from the same simulated particle.
- **T-Station ghost** if less than 70% of the T-Station hits originate from the same simulated particle.
- **Mismatch** if Velo and T-Station part are real tracks but belong to different simulated particles.

In table 6.2 the origin of the ghost tracks reconstructed offline and online as well as for tracks that composed a trigger candidate in the four body topological trigger is listed. The four body topological trigger selection was chosen because of its high output rate of more than 1 kHz and the high fraction of ghost candidates of more than 60%. Note that a track can, of course, suit into several of these categories, e.g., it can be a Velo (r-z) and at the same time a Velo 3D ghost.
It can be seen that in all three samples most of the ghost tracks are the result of a mismatched T-Station and Velo track part. In the online reconstruction however, the amount of ghosts due to mismatched parts is lower than in the offline reconstruction. In contrary, the fraction of ghost tracks containing a ghost T-Station part rises by 13%. Compared to the ghost origin on all online long tracks, the fraction of ghost tracks containing a Velo ghost is enhanced by 16.2% in tracks that formed a triggered HLT2 candidate. The explanation for this is that a misreconstructed track with wrong Velo

Table 6.3: Composition of the HLT2 trigger candidates in minimum bias events averaged over all selections. Candidates containing at least one ghost track are responsible for two thirds of the trigger rate.

origin	real partners	ghost tracks
uds quark hadrons	54.6%	84.3%
charm hadrons	11.2%	4.8%
beauty hadrons	34.2%	10.9%

hits has a high chance not to point precisely to the primary vertex and therefore pass the impact parameter cut in the trigger. The same applies for ghost tracks in the mismatch category.

6.1.3 Analysis of trigger candidates containing misreconstructed tracks

To figure out the composition of trigger candidates containing a misreconstructed track is necessary to understand the background of the HLT2 selections. Two questions are of particular interest:

- Which simulated particle has the largest hit contribution to the misreconstructed track?
- Which are the real tracks that acted as partners for the misreconstructed track to build a trigger candidate?

In Table 6.3 the Monte Carlo origin of real tracks of candidates that pass the four body topological trigger selection are shown. In addition to that, the origin of the simulated particle with the largest contribution to the misreconstructed track of the trigger candidate is shown. The majority of real tracks and ghost tracks come from prompt mesons and baryons composed of light quarks, mostly pions and kaons. If they would not contain a ghost track, such trigger candidates would fall to the categories of either prompt or pileup background as discussed in Chapter 6.1.1. A better estimate of the impact parameter of those tracks might help to identify them as prompt particles and suppress their selection rate.
About 11% of the real tracks originate from charm mesons or baryons. Since the topological trigger selections are designed to reconstruct charm and beauty mesons, those candidates would fall into one of the categories of signal, physics background, reflection background or background from $c\bar{c}$, if no misreconstructed track was used to form the candidate.
The fraction of real tracks used to form trigger candidates coming from beauty mesons or baryons is 34%. Those are tracks that are mainly used for physics analysis. Hence candidates containing these tracks would count as signal, physics background, reflection background or background from $b\bar{b}$ in the absence of the ghost track.
It can be concluded that even if the fraction of misreconstructed tracks was be reduced, it would be possible that events containing beauty or charm mesons would still be triggered because a real trigger candidate is then found in the event.

Chapter 7

Summary and Conclusion

In this thesis, the track reconstruction sequence for the second stage of the LHC*b* high level software trigger has been tuned to achieve the highest possible agreement with the offline tracking sequence.
The addition of a second pattern recognition algorithm for a three dimensional reconstruction of tracks in the vertex detector as well as of a redundant long track reconstruction algorithm enhance the relative track finding efficiency between online and offline reconstruction from 93% to 98%.
It was shown that the inclusion of hits in the trigger tracker in the long track reconstruction gives a handle on misreconstructed tracks. The final trigger output rate can be reduced by 7.5%, if information from the trigger tracker is used.
The resolution of the primary vertex can be improved to almost the offline performance, if a three dimensional vertex reconstruction is performed. This yields a better estimate of the impact parameter of the tracks and reduces the final trigger output rate by 6 to 11% depending on the reconstruction scenario.
It was pointed out that the usage of a fast Kalman filter based track fit in the online reconstruction can refine the momentum resolution of long tracks by 51% to almost the same as reached offline. The mass resolution in two body B decays improves from 48 MeV to 24 MeV. When the track fit is applied, the quality of the impact parameter estimate of real tracks is almost as good as offline. Additionaly, the reduced χ^2 of the track fit is an important quality variable to suppress misreconstructed tracks.
In the LHC*b* high level software trigger the refined Velo tracking as well as the inclusion of the information of the trigger tracker in the long track reconstruction will be applied per default. The three dimensional reconstruction of the primary vertex will be implemented in the trigger software. The improvements on the track parameter estimate and the reduced χ^2 of the track fit play a key role in HLT2 selections that use fitted tracks such as the topological trigger and the inclusive ϕ selections. The usage of the redundant long track reconstruction will be tested on data and should be considered if the necessary time is available.
The studies of the final trigger output candidates yield an important input for further efforts to improve the final trigger output rate. The variables shown can be combined to a track quality variable which can help to suppress misreconstructed tracks in problematic trigger selections.

Appendix A

Identification of misreconstructed tracks

To avoid triggering on candidates built from misreconstructed tracks one needs to find variables that have discriminating power to identify such tracks. Several considerations have to be made of such variables. First, the variables in question have to be available in the trigger at a reasonable amount of extra time. Secondly, they should be easy to tune and to understand on data. Finally, they should not impose any bias on physics quantities. Therefore, kinematic variables such as the momentum and the transverse momentum are not desirable for the discrimination of real tracks and ghost tracks.
In this section possible variables are discussed. Those variables can be roughly put into two categories: quality variables from the reconstruction process and variables including some hit information. None of that variables alone offer a clear separation between ghost tracks and real tracks. However, these variables can be combined to a more powerful selection criterion, As this is out of the scope of this thesis, it will be followed up in a later study [34].

A.1 Discriminating variables from pattern recognition

The pattern recognition algorithms already use internal quality variables to obtain an estimate of the quality of the track candidates. These variables can be used also in a combined ghost rejection variable. In Figure A.1 such variables are shown for ghost tracks and for real tracks.
The Velo pattern recognition uses a simple straight line fit to estimate the quality of the reconstructed track segments. This fit gives an estimate of the track quality. However, it does not take into account multiple scattering effects in the Velo as the Kalman filter based track fit does (see 3.2.1). The reduced χ^2 distribution is shown in figure A.1 (a). Misreconstructed tracks tend to have on average a slightly higher reduced χ^2 of the Velo fit.
The forward tracking uses several variables to decide on the quality of track candidates. One variable is the PatQuality. It combines information of the y separation between the Velo seed and the T-Station track candidate, the reduced χ^2 from a simple fit to the

T-Station part of the track and the momentum of the track (for a detailed discussion, see [23]). Smaller values of PatQuality indicate better tracks. In Figure A.1 (b) on can see that ghost tracks tend to have a higher value of the quality variable.
In addition, each pair of track candidates is examined if there is a possible clone T-Station track segment. In Figure A.1 (c) the number of track candidates for real and ghost tracks which are T-Station clones is shown. It can be seen that ghost tracks tend to form more likely candidates with the same T-Station segment than real tracks.
Track quality variables are also available for the backward tracking approach.
The reduced χ^2 from the Kalman track fit of the whole track was discussed in Chapter 5.2. It is the most powerfull discriminating variable, however, it is not necessarily available in the trigger.

A.2 Hit based discriminating variables

Besides the variables obtained from the pattern recognition algorithms, hit based variables can be used to distinguish real tracks from ghost tracks.
In figure A.2 (a) the number of hits on the track for ghost and real tracks is shown. It can be seen that real tracks have on average more hits on the track than ghost tracks.
Another variable to distinguish ghost and real tracks is the number of hits in the event. In busy events with a higher occupancy in the detector components the pattern recognition algorithms have a higher probability to produce misreconstructed tracks (see Figure A.2 (b)).
Figures A.2 (c) - (f) show the number of hits for real tracks and ghost tracks for Velo, trigger tracker, inner tracker and outer tracker. In all subdetectors, real tracks tend to have a higher number of hits than ghost tracks. This is due to the high efficiency of the detectors. In Figure A.2 (c) it can be seen that in the Velo an even number of hits is preferred. Because of the high efficiency of the Velo sensors, it is likely that both Velo r and ϕ sensor are hit in one station. In Figure A.2 (d) the number of TT hits on the tracks is shown. One can see that real tracks often have a TT track segment, while misreconstructed tracks have none. Because at least three hits in TT are required to form a track segment, there are no entries between zero and three hits. The importance of the TT hits to discriminate between good and bad tracks has already been discussed in Chapter 4.3. In Figures A.2 (e) and (f) it can be seen that also for the OT and IT real tracks have more hits than ghosts have. The peaks at zero hits originate from tracks that either pass through IT or OT alone. Besides the aforementioned simple hit based variables one can also look at the information of a pattern of multiple hits. Due to the high efficiency of the detectors it is very likely that there are, e.g., in the Velo hits in both r and ϕ sensors of the very same station and thus form a so called hit cluster. In addition it is very unlikely that there are many sensors without any hit, so called holes, between two hit sensors on the track. For misreconstructed tracks this assumption does not necessarily hold. In Figure A.3 the number of Velo clusters and Velo holes for real and ghost tracks is shown. It can be seen that those variables do have indeed some separating power.

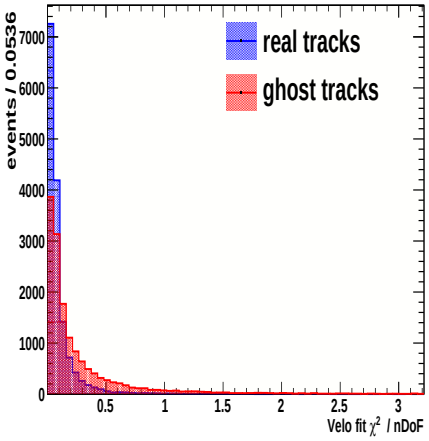

(a) Reduced χ^2 from the Velo track fit

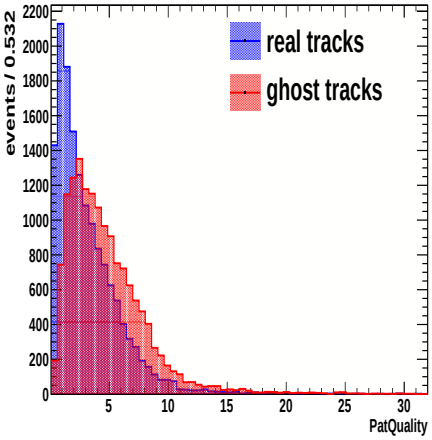

(b) PatQuality from `PatForward`

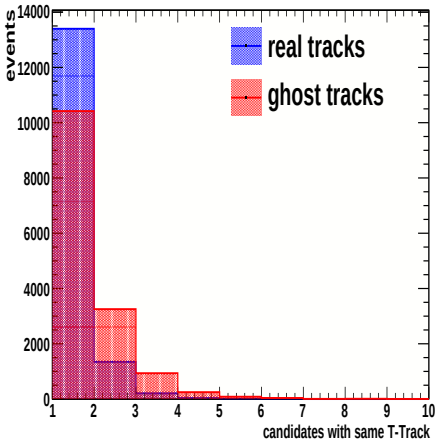

(c) Number of candidates with common T-Station parts

Figure A.1: Discriminating variables between ghost tracks and real tracks from pattern recognition algorithms. Shown are the internal quality variable and the number of track candidates with the same T-Station part from `PatForward` as well as the reduced χ^2 from the Velo pattern recognition.

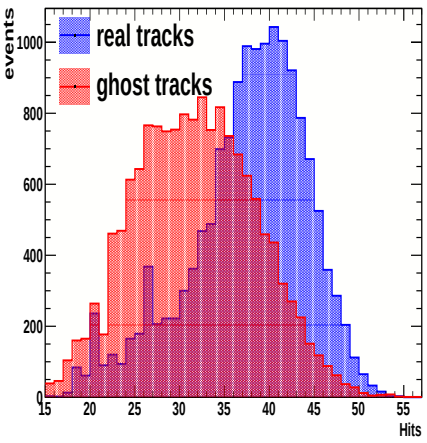

(a) Number of hits on the track

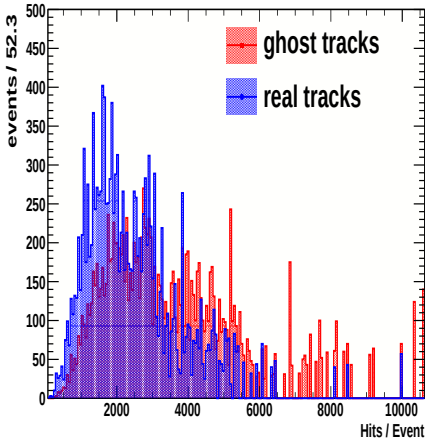

(b) Number of hits in the event

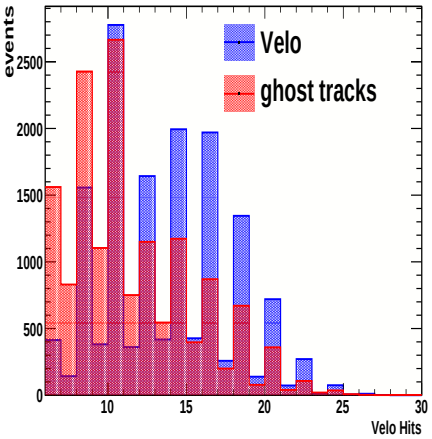

(c) Number of Velo hits

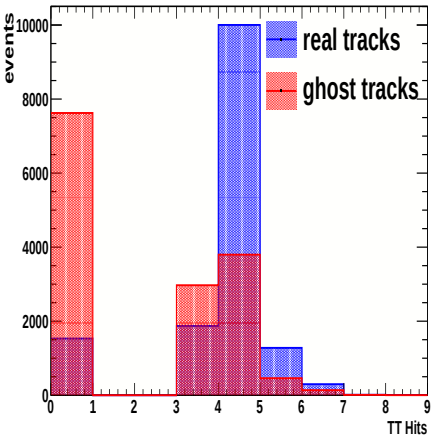

(d) Number of TT hits

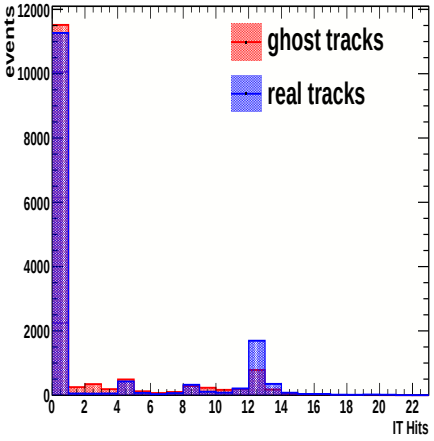

(e) Number of IT hits

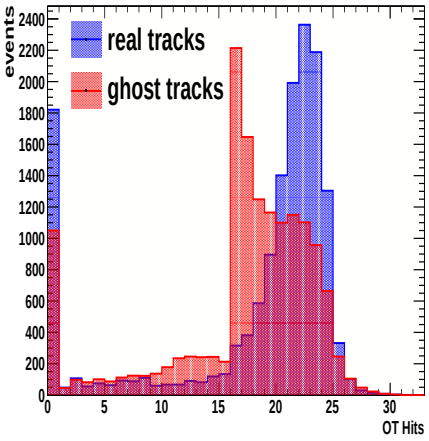

(f) Number of OT hits

Figure A.2: Hit based variables to discriminate between real tracks and ghost tracks. Shown are the overall hits on the track, as well as the number of hits in the event and the number of hits on the track in each subdetector. Real tracks on average have more hits on the track because of the high efficiency of the detectors as well as the higher probability to be a ghost for tracks with less hits. Crowded events with a high occupancy are more problematic as ghost tracks are concerned than normal events.

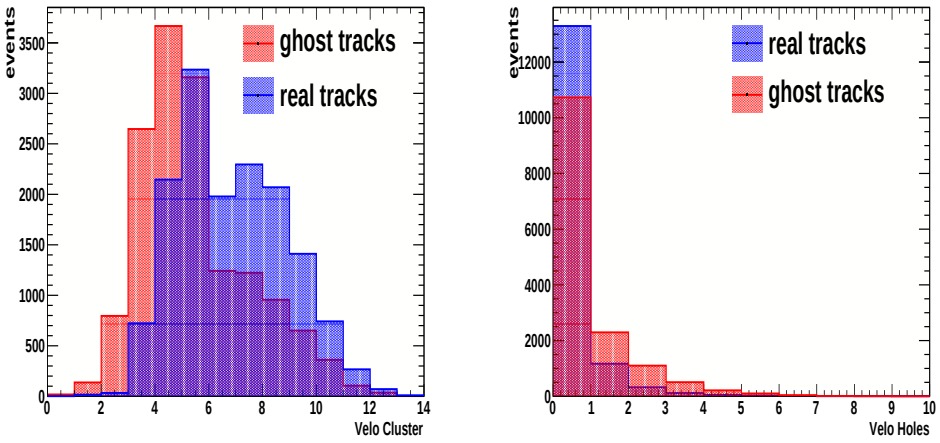

(a) Velo clusters (b) Velo holes

Figure A.3: Hit pattern based ghost variables. Shown are the number of Velo Clusters where both the Velo r and ϕ sensors are hit and the number of Velo holes, were a hit on the track between two hit sensors is missing. Hit pattern variables are available for all sub detectors.

Appendix B

Clone tracks in the HLT2

In addition to ghost tracks another form of misreconstructed tracks, the so called clone tracks, are produced by the pattern recognition. A clone track pair is a pair of two tracks that share 70% of the hits with each other. A clone track can occur, e.g., for real tracks, if a track is found independently by two different pattern recognition algorithms or if a track segment is used more than once to produce a track candidate. Also in the case of two particles traversing the detector close to each other and sharing a lot of hits on the tracks it is possible that clone tracks are produced. Clone track pairs can also occur in a pair of ghost tracks or combinations of a ghost track and a real track.
Since in the HLT2 redundant tracking algorithms run only on previously unused hits, no clone track pairs should be reconstructed. To analyse the pollution of the HLT2 long track sample with clone tracks, a sample of 2000 minimum bias events was searched for possible long track clones. Since misrecontructed Velo tracks and clone tracks introduced by mismatched Velo and T-Station part were found to be in particular important for the HLT2 (see 6.1.2) also a search for cloned Velo track segments was performed. For simplicity reasons, clone tracks produced in a HLT2 reconstruction scenario running only the forward trackingd was used in this study. A study on clone tracks from a combined seeding and matching approach was conducted and results will be discussed were necessary.
If one takes a look at the final track sample one finds that about 6.1% of the long tracks have a second track with which it shares at least 70% of its hits. In 4.0% of the cases a pair of long tracks have a cloned Velo track segment. By looking specifically at real tracks and ghost tracks, one can see that the fraction of tracks with a clone partner among the real tracks is about 4.4% for long clone tracks and 2.4% for cloned Velo track segments. For ghost tracks about 16.5% of the tracks are long track clones and 13.9% have a partner with an similar Velo clone segment. The overlap between Velo clones and long track clones is about 1.2% for real tracks and 2.4% for ghost tracks.
It is in particular interesting to look at the partners of both real and ghost tracks that were identified as clones in either the Velo or on the whole track. For real tracks 50.6% of the clone pairs consists of two real tracks, while in 49.4% of the cases one of the partners is a misreconstructed track. For ghost tracks 18.3% of the pairs contain two ghost tracks, whereas 81.7% contain a ghost and a real track. As 28% of all ghost tracks are either part of a long clone pair or a Velo clone pair, a search for such clone pairs seems worthwhile to reduce the amount of ghosts in the final track sample.

In a scenario with both forward and backward tracking a large amount of additional clone track pairs with a cloned Velo seed are produced. Such track pairs consist of a forward track and a match track that use the same Velo seed. In basically all of these track pairs, one track is real but the other one is a ghost. However, since the tuning of the online matching algorithm as presented in Chapter 4.4 avoids this problem, a separate investigation is not necessary. The addition of the backward tracking with a tuned matching procedure has been found to leave the clone fraction unchanged.

B.1 Identification and removal of clone tracks

All clone track pairs discussed so far have been produced by the forward tracking. Velo clones occour when either the Velo pattern recognition produces two tracks with a similar hit content, which is the case in 26% of the cases, or the same Velo seed is used twice in the forward tracking to produce a long track and both candidates are kept by the algorithm because they have a similar quality. This happens for 74% of the Velo clones.
A clone on the whole track happens most often, if the forward tracking finds similar T-Station tracks for two different Velo seeds and both candidates are kept because a decision about the track quality is not possible.
Several possible measures to find and remove cloned long tracks have been investigated. First it is possible to tune the forward tracking in a way that for each Velo seed only one candidate is kept. This will remove clone tracks were the same Velo seed is used twice to produce a long track. However, this has been found to be inefficient since there is no separation power between the real tracks and the ghost tracks available..
These results can be improved by using a dedicated clone killing algorithm after the pattern recognition to identify the clones. Such an algorithm exists for offline use (see Chapter 3.2.2) and has been tuned in terms of CPU time for the usage in HLT2 [35]. The advantage of such an algorithm is that it can use also the reduced χ^2 of a vertex fit if available. If such a clone killing algorithm is used after the pattern recognition and a track fit, the tracking efficiency drops from 93.5% to 92.8% on all long tracks while the event average ghost fraction decreases from 10.5% to 8.9%. The loss in efficiency comes from the fact that in a pair where a ghost and a real track are clone partners, in 26% of the cases the real track is discarded.
A further improvement of this might be possible if instead of using a ghost identification tool information about clones is added to a combined track quality variable as discussed in Chapter A. Information about clone T-Station parts from the forward tracking has already been discussed as possible discriminating variable and could be extended by information about possible Velo clones and clones on the whole track. As similar problems are expected in the offline reconstruction, this could also improve the ghost fraction of the offline forward tracking.

Bibliography

[1] Yao, W.-M. et al. *J. Phys.* **G33** , 1–1232 (2006, and 2007 partial update for the 2008 edition available on the PDG WWW pages (URL: `http://pdg.lbl.gov/`)).

[2] J. Van Tilburg. *Track simulation and reconstruction in LHCb.* CERN-THESIS-2005-020, (2005).

[3] CKMfitter group, J. Charles et al. *updated results and plots available at: http://ckmfitter.in2p3.fr.* Eur. Phys. J. C41, 1-131, hep-ph/0406184, (2009).

[4] Belle collaboration, K. Abe et al. *Improved measurement of direct CP violation in* $B \to K^+\pi^-$. Belle-Conf-0523, (2005).

[5] BaBar collaboration, B. Aubert et al. *Direct CP violation asymmetry in* $B \to K^+\pi^-$. Phys.Rev.Lett. **93, 131801**, (2004).

[6] A. Lenz, U. Nierste . *Theoretical Update on* B_s-$\overline{B}_s$ *Mixing.* hep-ph/0612167v3, (2006).

[7] J. Albrecht et al. *Road map for the measurement of mixing induced CP violation in* $\mathrm{B_s} \to \mathrm{J}/\psi\phi$ *at LHCb.* LHCb/ROADMAP3-001 document in preparation, (2009).

[8] The CDF collaboration. *First Flavor-Tagged Determination of Bounds on Mixing-Induced CP Violation in* $\mathrm{B_s} \to \mathrm{J}/\psi\phi$ *Decays.* Phys. Rev. Lett. 100, 161802, (2008).

[9] The CDF collaboration. *An updated measurement of the CP violating phase* Φ_s. CDF/ANAL/BOTTOM/PUBLIC/9458, (2009).

[10] The D0 collaboration. *Measurement of Bs mixing parameters from the flavor-tagged decay* $\mathrm{B_s} \to \mathrm{J}/\psi\phi$. hep-ex, arXiv:0802.2255v1, (2008).

[11] E. Barberino et al. *Heavy Flavour Averaging Group.* `http://www.slac.stanford.edu/xorg/hfag`.

[12] D. Martinez et al. *Analysis of the decay* $\mathrm{B_s} \to \mu^+\mu^-$ *at LHCb.* LHCb/ROADMAP1-002 document in preparation, (2009).

[13] T. Aaltonen et al, C. C. *Physical Review Letters* **100**(10), 101802 (2008).

[14] The LHCb Collaboration. *The LHCb Detector at the LHC.* 2008 JINST 3 S08005.

[15] The LHCb collaboration. *LHCb Inner Tracker design report.* CERN-LHCC/2002-029, (2003).

[16] The LHCb Collaboration. *LHCb Outer Tracker Technical Design Report.* CERN/LHCC-2001-024, (2001).

[17] G. v. Apeldoorn et al. *Beam Tests of Final Modules and Electronics of the LHCb Outer Tracker in 2005.* LHCb/PUB-2005-076, (2005).

[18] The LHCb Collaboration. *LHCb Calorimeters Technical Design Report.* CERN/LHCC-2000-036.

[19] The LHCb Collaboration. *LHCb Trigger System Technical Design Report.* CERN/LHCC-2003-031.

[20] The LHCb Collaboration. *LHCb Muon Technical Design Report.* CERN/LHCC-2000-037.

[21] Albrecht, J. *Fast Track Reconstruction for the High Level Trigger of the LHCb Experiment. CERN-THESIS-2009-120.* PhD thesis, University of Heidelberg. July 2009.

[22] M. Schiller. *LHCb tracking Twiki page.* `https://twiki.cern.ch/twiki/view/LHCb/LHCbTrackingStrategies`, (2008).

[23] S. Hansmann-Menzemer, O. Callot. *The Forward Tracking: Algorithm and Performance Studies.* CERN-LHCb-2007-015, (2007).

[24] Forty, R., Needham, M. *Standalone Track Reconstruction in the T-Stations.* CERN-LHCb-2007-022, (2007).

[25] Schiller, M. *Standalone track reconstruction for the outer tracker of the LHCb experiment using a cellular automaton.* Diploma Thesis, Universitat Heidelberg, (July 2007).

[26] Kalman, R.E. *A new approach to linear filtering and prediction problems.* Trans. ASME J. Bas. Eng. **D82** (1960) 35.

[27] Frühwirth, R. *Application of Kalman Filtering to track and vertex fitting.* Nucl. Instrum. Meth. A **262** (1987) 444.

[28] R. Van der Eijk. *Track reconstruction in the LHCb experiment.* CERN-THESIS-2002-032, (2005).

[29] A. Perieanu. *A Fast Algorithm to Identify and Remove Clone Tracks.* LHCb-2008-020, (2008).

[30] T. Nakada et al. *HLT Physics meeting.* 19. May 2009, CERN, Geneva.

[31] Gandelman, M. *L0xHlt1 DC06 BW-division.* Presented at LHC*b* collaboration meeting, 28. May 2009.

[32] Callot, O., Schiller, M. *Pat Seeding: A Standalone Track Reconstruction Algorithm.* CERN-LHCb-2008-042, (2008).

[33] V. Gligorov. *BackgroundCategory Tool - Information from DaVinci class reference.* From the DaVinci Doxygen documentation.

[34] J. Albrecht, G. Krocker. *Neural Net Based Track Quality Variable.* Presentation at LHCb TRec meeting, (12. October 2009).

[35] G. Krocker. *HLT2 tracking sequence.* Presented at the LHC*b* collaboration meeting, 28. May 2009.

Erklärung

Ich versichere, dass ich diese Arbeit selbständig verfasst und keine anderen als die angegebenen Quellen und Hilfsmittel benutzt habe.

Heidelberg, den 01. November 2009 _____